

A Hubble Space Telescope Imaging Survey of Low-Redshift Swift-BAT Active Galaxies*

MINJIN KIM,¹ AARON J. BARTH,² LUIS C. HO,^{3,4} AND SUYEON SON¹

¹*Department of Astronomy and Atmospheric Sciences, Kyungpook National University, Daegu 702-701, Korea; mkim.astro@gmail.com*

²*Department of Physics and Astronomy, 4129 Frederick Reines Hall, University of California, Irvine, CA 92697-4575, USA*

³*Kavli Institute for Astronomy and Astrophysics, Peking University, Beijing 100871, China; lho.pku@gmail.com*

⁴*Department of Astronomy, School of Physics, Peking University, Beijing 100871, China*

ABSTRACT

We present initial results from a Hubble Space Telescope snapshot imaging survey of the host galaxies of Swift-BAT active galactic nuclei (AGN) at $z < 0.1$. The hard X-ray selection makes this sample relatively unbiased in terms of obscuration compared to optical AGN selection methods. The high-resolution images of 154 target AGN enable us to investigate the detailed photometric structure of the host galaxies, such as the Hubble type and merging features. We find that 48% and 44% of the sample is hosted by early-type and late-type galaxies, respectively. The host galaxies of the remaining 8% of the sample are classified as peculiar galaxies because they are heavily disturbed. Only a minor fraction of host galaxies (18%–25%) exhibit merging features (e.g., tidal tails, shells, or major disturbance). The merging fraction increases strongly as a function of bolometric AGN luminosity, revealing that merging plays an important role in triggering luminous AGN in this sample. However, the merging fraction is weakly correlated with the Eddington ratio, suggesting that merging does not necessarily lead to an enhanced Eddington ratio. Type 1 and type 2 AGN are almost indistinguishable in terms of their Hubble type distribution and merging fraction. However, the merging fraction of type 2 AGN peaks at a lower bolometric luminosity compared with those of type 1 AGN. This result may imply that the triggering mechanism and evolutionary stages of type 1 and type 2 AGN are not identical.

Keywords: galaxies: active — galaxies: bulges — galaxies: fundamental parameters — galaxies: photometry — quasars: general

1. INTRODUCTION

In massive galaxies that exhibit bulges, supermassive black holes (SMBHs) are ubiquitous. The strong correlations between SMBH mass and the physical properties (e.g., luminosity, velocity dispersion, and stellar mass) of the spheroidal component of the host galaxy imply a causal connection between a SMBH and its host galaxy in terms of their formation and evolution (Magorrian et al. 1998; Gebhardt et al. 2000; Ferrarese & Merritt 2000; Kormendy & Ho 2013). According to theoretical studies, active galactic nuclei (AGN) that originate from accreting SMBH play an important role in regulating BH growth and star formation, which, in turn, can produce the strong correlations

between SMBHs and the properties of their host galaxies (Fabian 1999; Di Matteo et al. 2005; Hopkins et al. 2005). In this model, SMBH growth and star formation occur primarily during the AGN phase, which can be triggered by gas-rich mergers or interactions with companion galaxies (Sanders et al. 1988; Hopkins et al. 2008). Therefore, identifying the merging features of AGN hosts is vital to understand the galaxy–host connection.

According to the AGN unification model, the accretion disk and broad-line region are directly observed in type 1 AGN, while those central structures are visually obscured by the sub-parsec dusty torus in type 2 AGN (Antonucci 1993; Urry & Padovani 1995). On the contrary, if an AGN is mainly triggered by gas-rich merging, then the gas and dust content in the central regions of the host can be enhanced during the early stages of the merger (Blecha et al. 2018). A late stage then occurs, in which the AGN-driven outflow can expel the surrounding gas and dust so that the AGN is

* Based on observations made with the NASA/ESA Hubble Space Telescope, obtained at the Space Telescope Science Institute, which is operated by the Association of Universities for Research in Astronomy, Inc., under NASA contract NAS5-26555. These observations are associated with program #15444.

eventually observed to be type 1 (Sanders et al. 1988; Ishibashi & Fabian 2016). Therefore, the nucleus can be naturally obscured due to the dense material in the host galaxy on spatial scales larger than the dusty torus. According to this evolutionary sequence, the host galaxies of type 2 AGN are more likely to be disturbed than those of type 1 AGN, or might show an association with earlier merger stages. On the other hand, Elitzur et al. (2014) argued that type 1 AGN can evolve to intermediate-type (1.8-1.9), and finally to type 2 AGN as luminosity decreases. In this light, investigating the physical properties of host galaxies is crucial not only to determine the AGN triggering mechanism but also to test AGN unification models. Host galaxy properties have been used to test unified models for many AGN samples (e.g., Simcoe et al. 1997). Several studies have found that the merging fraction for obscured AGN is higher than that for unobscured AGN (e.g., Urrutia et al. 2008; Glikman et al. 2015; Donley et al. 2018). Additionally, Compton-thick AGN appear to be preferentially hosted by merging galaxies (Kocevski et al. 2015; Ricci et al. 2017b; Koss et al. 2018). Koss et al. (2011), however, argued that the properties of the host galaxies of type 1 and type 2 AGN are indistinguishable.

Numerous studies have investigated the properties of host galaxies of nearby and distant AGN. One of the primary goals of those studies is to identify the merging features in the AGN hosts as a possible origin of AGN triggering. Several studies have claimed that nearby AGN are preferentially hosted by galaxies that exhibit merging features compared with normal galaxies (Koss et al. 2011; Hong et al. 2015; Goulding et al. 2018; Ellison et al. 2019; Marian et al. 2020). In addition, luminous AGN are more likely to be associated with merging or interaction than less luminous AGN (e.g., Treister et al. 2012; Kim et al. 2017). However, some observational studies have found that there is no evidence of an excess of merging fraction in various types of luminous AGN (e.g., Dunlop et al. 2003; Cisternas et al. 2011; Böhm et al. 2013; Villforth et al. 2014, 2017). For example, Zhao et al. (2019) argued that only a minor fraction Type 2 quasar hosts (34%) are mergers, suggesting that major merging plays only a limited role in triggering AGN. For narrow-line Seyfert 1 (NLS1) galaxies, the fraction of barred hosts is significantly higher than the bar fraction of ordinary Type 1 AGN, implying that this subclass is predominantly triggered by internal secular evolution rather than by merging (Crenshaw et al. 2003; Deo et al. 2006; Sani et al. 2010; Orban de Xivry et al. 2011; Kim et al. 2017).

Finally, the photometric properties of host galaxies have been widely used to explore the coevolution be-

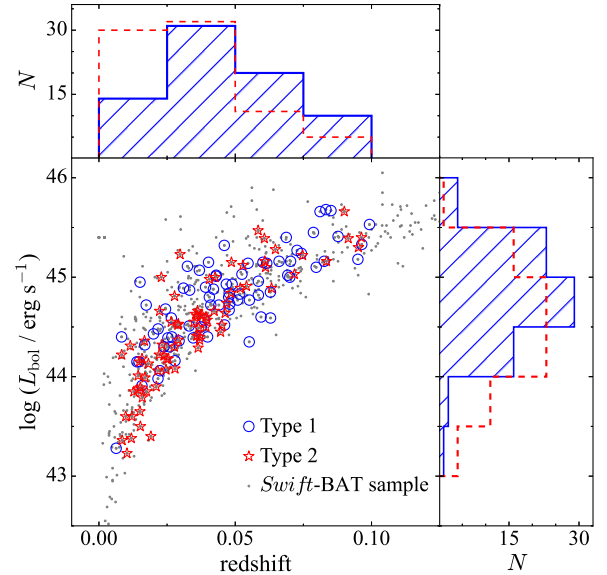


Figure 1. Redshift and bolometric luminosity distributions of the parent sample of Swift-BAT AGN (small gray dots). The Type 1 AGN observed for this HST program are denoted by blue stars and blue histograms, while Type 2 objects are given by red circles and red histograms. Bolometric luminosity is estimated from the intrinsic X-ray luminosity (Ricci et al. 2017) assuming a bolometric correction of 8.

tween SMBHs and host galaxies. The stellar populations of AGN host galaxies can provide a useful constraint on the SMBH-galaxy connection (e.g., Sánchez et al. 2004; Canalizo & Stockton 2013; Matsuoka et al. 2014; Kim & Ho 2019; Zhao et al. 2019). Some studies have shown that host galaxies of type 1 AGN tend to be bluer or overluminous compared with inactive galaxies due to the former’s young stellar population (e.g., Sánchez et al. 2004; Kim & Ho 2019). However, other investigations have found no sign of young stellar populations in AGN hosts (e.g., Nolan et al. 2001; Bettoni et al. 2015). Additionally, the spheroid luminosity of type 1 AGN hosts has also been used to investigate the relation between BH mass (M_{BH}) and bulge luminosity (L_{bul}) (e.g., Kim et al. 2008; Greene et al. 2010; Park et al. 2015; Kim & Ho 2019; Li et al. 2021).

The aforementioned studies have employed widely different sample selection methods and datasets with diverse properties in terms of wavelength or filter bands, spatial resolution, and depth, and these differences may be largely responsible for the sometimes divergent conclusions reached in different investigations. Thus, despite the large observational effort invested into AGN host galaxy studies over many years, further work based on large, uniformly selected samples with high-quality imaging data can still provide new insights. Indeed,

there have been several attempts to conduct imaging surveys of nearby Seyferts using HST (e.g., Nelson et al. 1996; Malkan et al. 1998; Schade et al. 2000). Those surveys used early HST images with a relatively narrow field of view that did not always cover the full host galaxy (the Wide Field Planetary Camera 1 and 2), and early snapshot programs with these cameras obtained relatively shallow depth. Images of Type 1 AGN are often saturated due to the bright nuclei, which makes it difficult to obtain a robust decomposition to determine bulge properties accurately. Furthermore, some of these studies (e.g., Malkan et al. 1998) observed samples selected from highly heterogeneous criteria based on AGN catalogs available at the time.

To overcome these limitations, we have used HST to conduct an imaging survey of nearby AGN at $z < 0.1$ selected from the Swift-BAT AGN catalog. Swift-BAT AGN are identified from hard X-ray data that, compared with optical and infrared data, is less affected by extinction and contamination from star formation. Therefore, hard X-ray data provides a relatively uniform and homogeneous sample in terms of obscuration, with the exception of very highly obscured (Compton-thick) AGN. The deep and coherent high-resolution imaging dataset from HST allows us to robustly investigate the structural properties of the host galaxies for a large and uniformly selected sample. Moreover, the Swift-BAT AGN sample has the benefit of extensive multiwavelength measurements (e.g., BH mass, bolometric luminosity, Eddington ratio, hydrogen column density, and optical classification) that have been carried out in numerous studies (Koss et al. 2017; Oh et al. 2017; Ricci et al. 2017a). Hence, our imaging survey is an excellent complement to the existing body of data for this benchmark AGN sample, providing an excellent dataset to study the detailed properties of nearby AGN hosts and to investigate the relationships between AGN and host properties while minimizing sample selection biases.

This paper presents a description of the morphological properties of the host galaxies of these low- z Swift-BAT AGN using newly acquired HST I -band images for 154 objects. Our primary goal is to explore the connection between the physical properties of AGN and those of their hosts. Section 2 describes the sample selection, our imaging data, and the physical properties of the sample. Section 3 presents visual morphological classifications. We discuss the correlation between the morphological structures of the hosts and the properties of the AGN in Section 4. A summary is given in Section 5. This work adopts the following cosmological parameters: $H_0 = 100h = 67.8 \text{ km s}^{-1} \text{ Mpc}^{-1}$, $\Omega_m = 0.308$, and $\Omega_\Lambda = 0.692$ (Planck Collaboration et al. 2016).

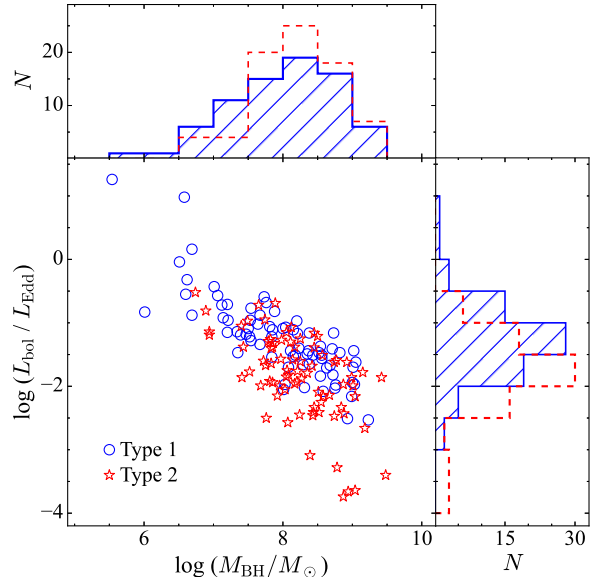


Figure 2. The distributions of BH mass and Eddington ratio of the sample. M_{BH} is measured using the virial method, the $M_{\text{BH}} - \sigma_*$ relation, or the $M_{\text{BH}} - M_*$ relation.

2. SAMPLE AND DATA

2.1. Sample Selection

In 2017, the Space Telescope Science Institute announced a special mid-cycle call proposals for “gap-filler” snapshot surveys to be conducted using the Advanced Camera for Surveys (ACS) Wide-Field Camera (WFC). The programmatic goal for this call was to provide large, full-sky catalogs of snapshot targets that would be used to fill HST scheduling gaps, at lower priority than standard general observer and snapshot programs. This survey (HST program 15444) was selected as one of three gap-filler programs in the 2017 call. The proposal call dictated that the total duration of snapshot visits should be $\lesssim 26$ minutes, which is sufficient to allow for two full-frame ACS/WFC exposures with a total on-source exposure time of ~ 700 s after acquisition and other overheads.

Our sample is drawn from the 70-month Swift-BAT X-ray source catalog (Baumgartner et al. 2013). Since our primary science goals involve morphological studies of AGN host galaxies, we focus on low-redshift objects, and we selected Swift-BAT AGN at $z < 0.1$. After cross-matching this catalog with the HST archive, we excluded objects already having images in an I -band equivalent filter (in most cases F814W) with the WF/PC2, ACS, or WFC3 cameras, to avoid duplications. The remaining set of 543 objects provides an ideal gap-filler sample with a large number of targets widely distributed over the full sky. No cuts to the sample were made based on

Galactic latitude or foreground extinction, because HST *I*-band imaging could in principle provide new morphological classifications and host galaxy structural information even for targets in fields with moderate to high extinction that otherwise might not be observed in other surveys. Figure 1 shows the distribution of redshifts and bolometric luminosities for the parent Swift-BAT sample and for the set of 543 targets making up the sample for program 15444.

2.2. Observations

Observations for Program 15444 began in 2018 March and are ongoing (at a low rate) during the first half of 2021. This paper includes data taken through 2021 June. We used ACS/WFC with the F814W filter, which is approximately equivalent to the *I* band, to maximize the brightness contrast between the host galaxy and the active nucleus. Suffering less dust attenuation than filters at shorter wavelengths, F814W also allows us to better probe the photometric substructures of the hosts. We obtained two dithered exposures per target with integration times of 337 s, the minimum time required to avoid buffer dump overheads. The AGN was centered on the WFC1 detector. For Type 1 (unobscured) AGN, a nuclear point source is generally expected to be present at optical wavelengths (Nelson et al. 1996). Accordingly, we took an additional 5 s exposure with the WFC1-B512 subarray to obtain an unsaturated image of the nuclear point source and its immediate surroundings for objects listed as Type 1 AGN by Baumgartner et al. (2013) or Koss et al. (2017). Of the 157 AGN targeted for observations, useful data were obtained for 154 sources (Table 1), while three observations were lost due to guide star acquisition failures. For other targets, delayed guide star acquisition led to slightly shorter exposure times than the planned 2×337 s (SWIFT J0533.9–1318, SWIFT J0747.5+6057, and SWIFT J0753.1+4559). The set of 154 successfully observed targets includes 75 Type 1 and 79 Type 2 AGN.

2.3. Data Reduction

For the long exposures, we adopt the standard reduction provided by the pipeline, including bias and dark subtraction, flat-field correction, and correction for charge-transfer efficiency. The cosmic ray rejection was performed when combining the two dithered images is imperfect. Therefore, we additionally applied the LACosmic algorithm (van Dokkum 2001) to the individual images to improve the cosmic ray rejection. We used the PyRAF task TWEAKREG to determine a robust shift between the dithered images. The final combined images, generated with ASTRODRIZZLE, have a pixel scale

of $\sim 0''.05$ and a field-of-view of $\sim 202'' \times 202''$. We measured the variance of the sky values after masking all objects to determine the depth of the images, which on average we estimate to be ~ 23.6 mag arcsec $^{-1}$ (1σ).

The short-exposure sub-array images for the type 1 objects exhibit horizontal bands introduced by bias striping noise (Grogan et al. 2010, 2011), which were removed separately with the ACS_DESTRIPE_PLUS TASK. The saturated pixels in the combined long-exposure image were replaced with the same pixels in the short, unsaturated image. The short and long exposures were aligned using the position of the nucleus. The central position of the nucleus for the long exposures was determined after masking the saturated pixels.

2.4. Physical Properties of AGN

To investigate the connection between AGN and their host galaxies, we assembled the optical spectral properties of the sample from the literature to estimate physical properties such as BH mass, accretion rate, and bolometric luminosity. For type 1 AGN, we use the virial method ($M_{\text{BH}} \propto Rv^2/G$) to estimate BH mass by combining the size (R_{BLR}) and velocity dispersion (v) of the broad-line region (BLR). The BLR size can be estimated through reverberation mapping experiments (Blandford & McKee 1982) and from single-epoch optical spectroscopy using the empirical relation between R_{BLR} and AGN luminosity (Kaspi et al. 2000; Bentz et al. 2013). The intrinsic scatter of the BLR size-luminosity relation (Du et al. 2018; Fonseca Alvarez et al. 2020) introduces significant systematic uncertainty into the BH masses derived from single-epoch spectra. For single-epoch mass estimates, the assumption of a single virial scaling factor contributes additional error to the mass estimates, since the true virial factor for a given AGN will depend on the geometry and kinematics of the BLR. While the mean virial factor has been determined by assuming that AGN follow the same $M_{\text{BH}} - \sigma_*$ relation as the inactive galaxies, its calibration appears to be sensitive morphologies of galaxies and types of AGNs (e.g., Ho & Kim 2014). Here, we recalculate the BH masses rather than using the values from Koss et al. (2017). We adopt the virial mass estimator based on H β and 5100 Å AGN continuum luminosity as calibrated by Ho & Kim (2015) for all bulge types, using spectral measurements from Koss et al. (2017) of 56 type 1 AGN. We use the scaling relations of Greene & Ho (2005) to convert H α and H β luminosities to 5100 Å AGN luminosity, and we scale broad H α line widths and broad H β line widths.

For the Type 1 AGN lacking useful measurements of broad emission lines but that do have available stellar

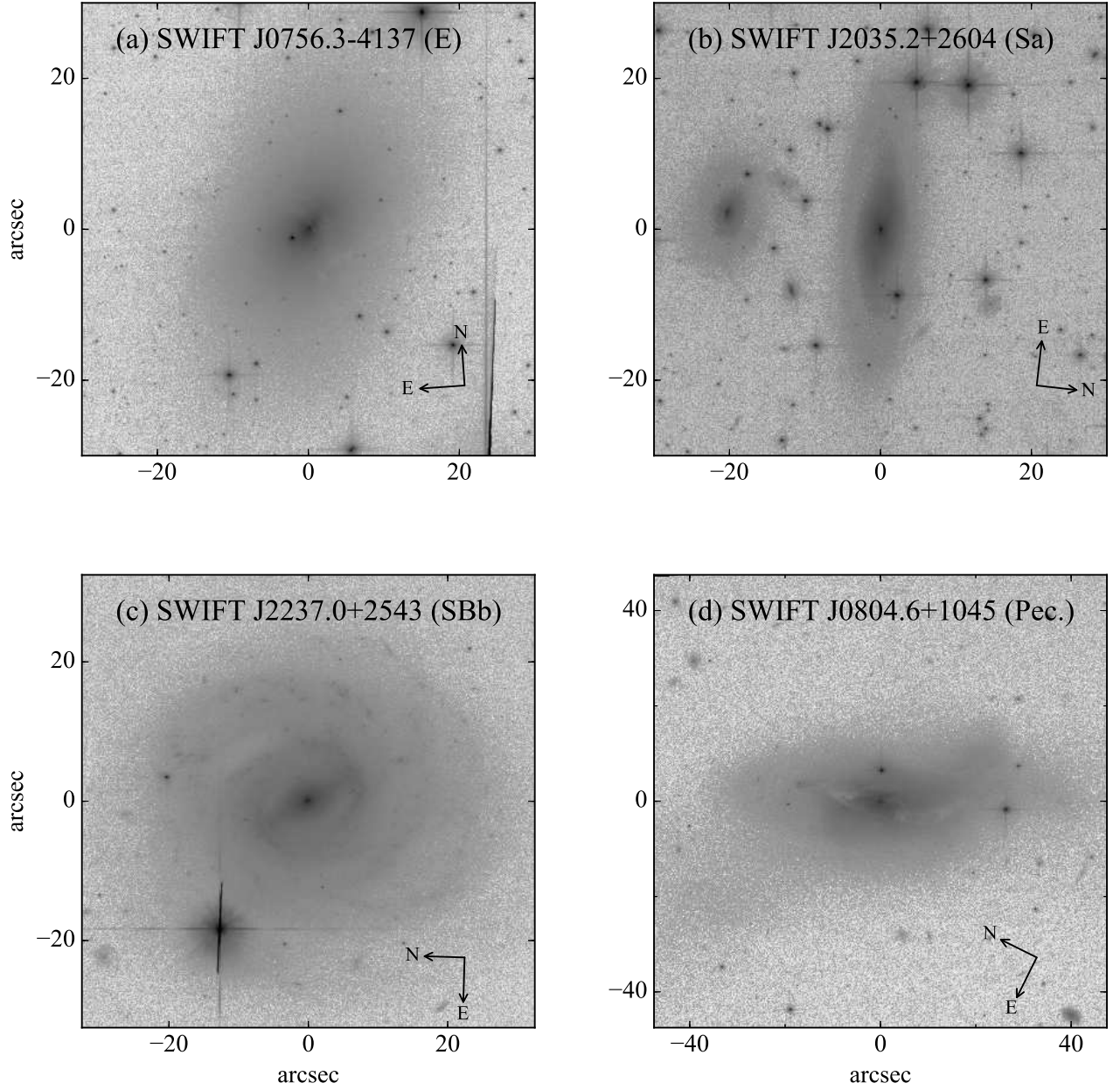


Figure 3. Representative examples of various morphological types: (a) elliptical, (b) Sa spiral, (c) barred SBb spiral, and (d) peculiar. All images are displayed on an asinh stretch.

velocity dispersion (σ_*) measurements, and for Type 2 objects having σ_* available, we compute M_{BH} using the $M_{\text{BH}} - \sigma_*$ relation from [Kormendy & Ho \(2013\)](#)¹.

For the remaining 63 objects without broad-line measurements or information on σ_* , we estimate M_{BH} from

¹ We use the $M_{\text{BH}} - \sigma_*$ relation for classical bulges and elliptical galaxies: $\log(M_{\text{BH}}/M_\odot) = 8.49 + 4.38 \log(\sigma_*/200 \text{ km s}^{-1})$.

the total stellar mass of the host galaxy (M_*). Although the $M_{\text{BH}} - M_*$ relation is not as tight as the $M_{\text{BH}} - \sigma_*$ relation, it can still yield approximate BH masses. The $M_{\text{BH}} - M_*$ relation is sensitive to the host galaxy morphological type. For the sake of simplicity, we adopt the $M_{\text{BH}} - M_*$ relation for all galaxy types, which has an uncertainty of ~ 0.8 dex ([Greene et al.](#)

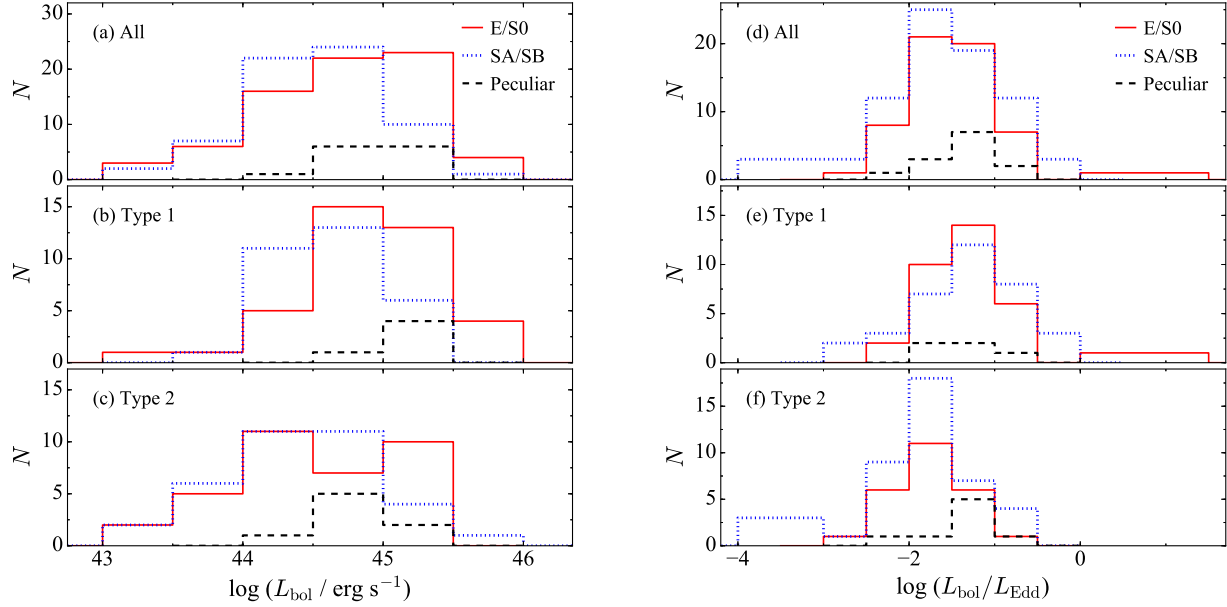


Figure 4. The distributions of bolometric luminosity (L_{bol}) and Eddington ratio ($L_{\text{bol}}/L_{\text{Edd}}$) for different morphological classifications. The red, blue, and black histograms denote early-type galaxies (E/S0), late-type galaxies with spiral arms (SA/SB), and peculiar galaxies, respectively.

2020)². We obtain the integrated F814W-band flux of the host galaxy through elliptical isophotal fitting of the observed images using the IRAF task *ellipse*, after masking blended nearby galaxies and foreground stars using SExtractor (Bertin & Arnouts 1996). For type 1 AGN, the nucleus is subtracted prior to isophotal fitting using the point-spread function generated from isolated stars in the science images (S. Son et al., in preparation). The *I*-band flux is corrected for Galactic extinction (Schlafly & Finkbeiner 2011), and a *k*-correction is applied according to the method described by Chilingarian et al. (2010) using host galaxy $V - I_C$ colors assigned based on the morphological classification (Section 4.1; Fukugita et al. 1995). Along with the mass-to-light ratio inferred from the $V - I_C$ color (Into & Portinari 2013), the integrated *I*-band luminosity then gives M_* .

Note that assigning a fixed color based on galaxy morphology likely overestimates the true stellar mass if AGN host galaxies preferentially contain a younger stellar population (Sánchez et al. 2004; Zhao et al. 2019), especially in systems with higher Eddington ratio (Kim & Ho 2019). However, apart from later-type spirals with pseudo bulges (Zhao et al. 2021), the effect of young stars may not be substantial in the *I* band. Pseudo bulges contribute $\lesssim 20\%$ to the total light in disk galax-

ies (e.g., Gao et al. 2019). This, in conjunction with the fact that our sample has relatively low Eddington ratios (median $\langle \log L_{\text{bol}}/L_{\text{Edd}} \rangle = -1.5$), leads us to suspect that the systematic uncertainty due to mass-to-light ratio should be small compared with the intrinsic scatter in the $M_{\text{BH}} - M_*$ relation.

We use the intrinsic hard X-ray (14 – 195 keV) luminosity derived from spectral fitting of the Swift-BAT data by Ricci et al. (2017a) to estimate the bolometric luminosity using a conversion factor of 8 (Koss et al. 2017; Ricci et al. 2017a)³. The AGN bolometric luminosities range from $L_{\text{bol}} = 10^{43.2} - 10^{45.7} \text{ erg s}^{-1}$, and, for Eddington luminosity $L_{\text{Edd}} = 1.26 \times 10^{38} (M_{\text{BH}}/M_{\odot}) \text{ erg s}^{-1}$, the Eddington ratios span $L_{\text{bol}}/L_{\text{Edd}} = 0.00018 - 18.2$. Finally, we take the column density of neutral hydrogen (N_{H}) deduced from spectral analysis of the X-ray data, as assembled by Ricci et al. (2017a). A lower limit of $N_{\text{H}} \approx 10^{20} \text{ cm}^{-2}$ yields negligible obscuration along the line of sight. The distributions of BH mass and Eddington ratio are displayed in Figure 2. The comparison reveals that the BH masses of type 2 AGN are systematically higher than those of type 1 by ~ 0.16 dex. However, given the uncertainties of BH mass measurements (0.3–0.8 dex) and the different methods applied for the two populations, it is unclear if this represents a genuine difference between the type 1 and type 2 subsamples.

² We use the $M_{\text{BH}} - M_*$ relation for all galaxy types: $\log(M_{\text{BH}}/M_{\odot}) = 7.43 + 1.61 \log(M_*/3 \times 10^{10} M_{\odot})$.

³ X-ray measurements are unavailable for SWIFT J1737.7–5956A.

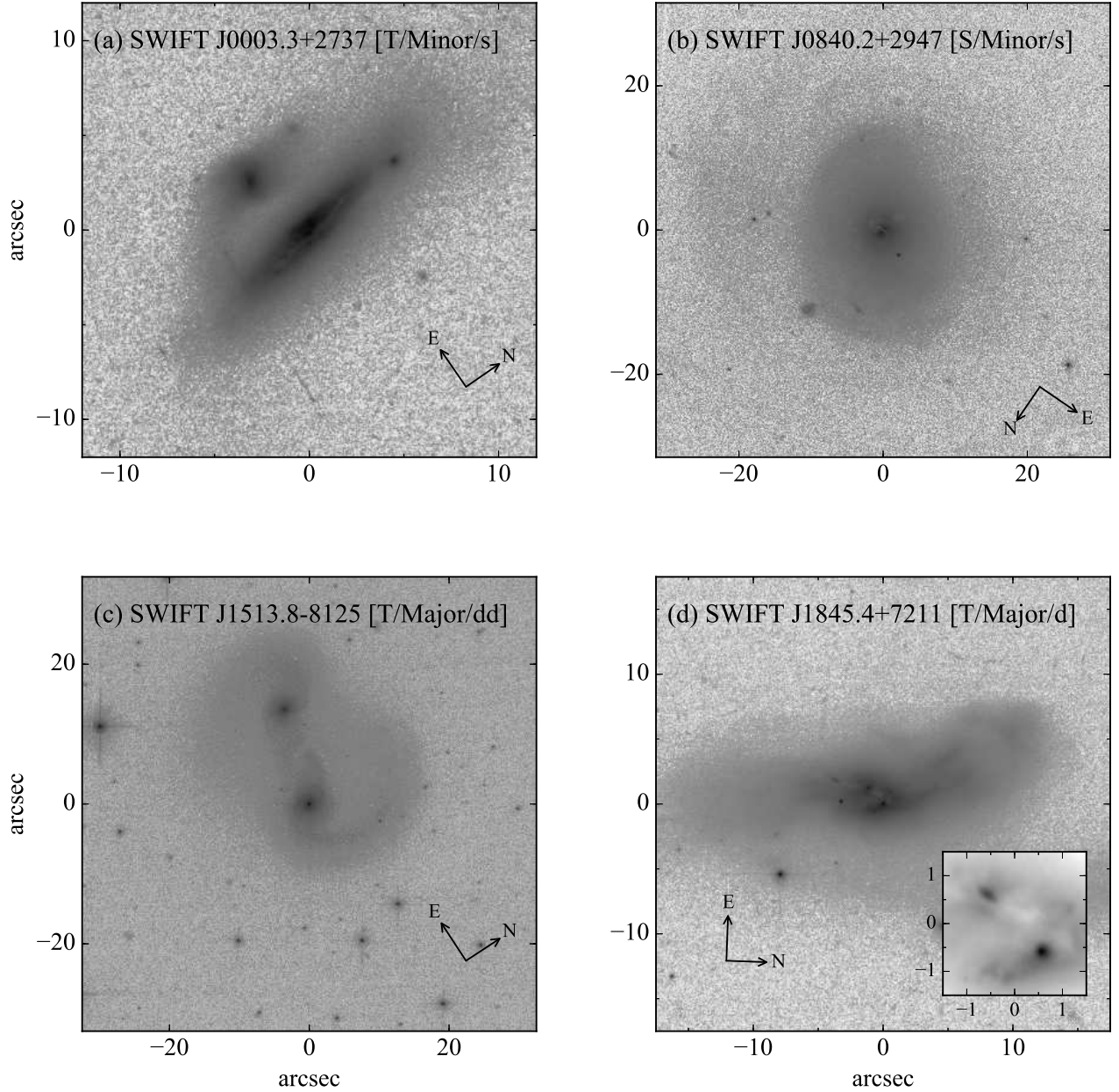


Figure 5. Example images of subgroups based on the various merging properties: (a) minor merger with tidal tail and single nucleus; (b) minor merger with shell and single nucleus; (c) major merger with tidal tail and double nuclei in separate hosts; and (d) major merger with tidal tail and double nuclei in a single host. In panel (d), a close-up of the central region is shown in the inset.

Finally, we also estimate the axis ratio (b/a , where b is the semi-minor axis and a is the semi-major axis) of the host galaxy using the results from the elliptical isophotal analysis.

3. ANALYSIS AND RESULTS

3.1. Morphological Classification

All the targets are classified into approximate morphological types, based on visual inspection independently conducted by three of the authors (MK, AB, LH). We assign the morphologies into four basic Hubble types: elliptical (E), lenticular (S0), spiral (S), and peculiar. The disk galaxies are additionally scrutinized for the possible presence of a bar (SA/SB) and the relative prominence

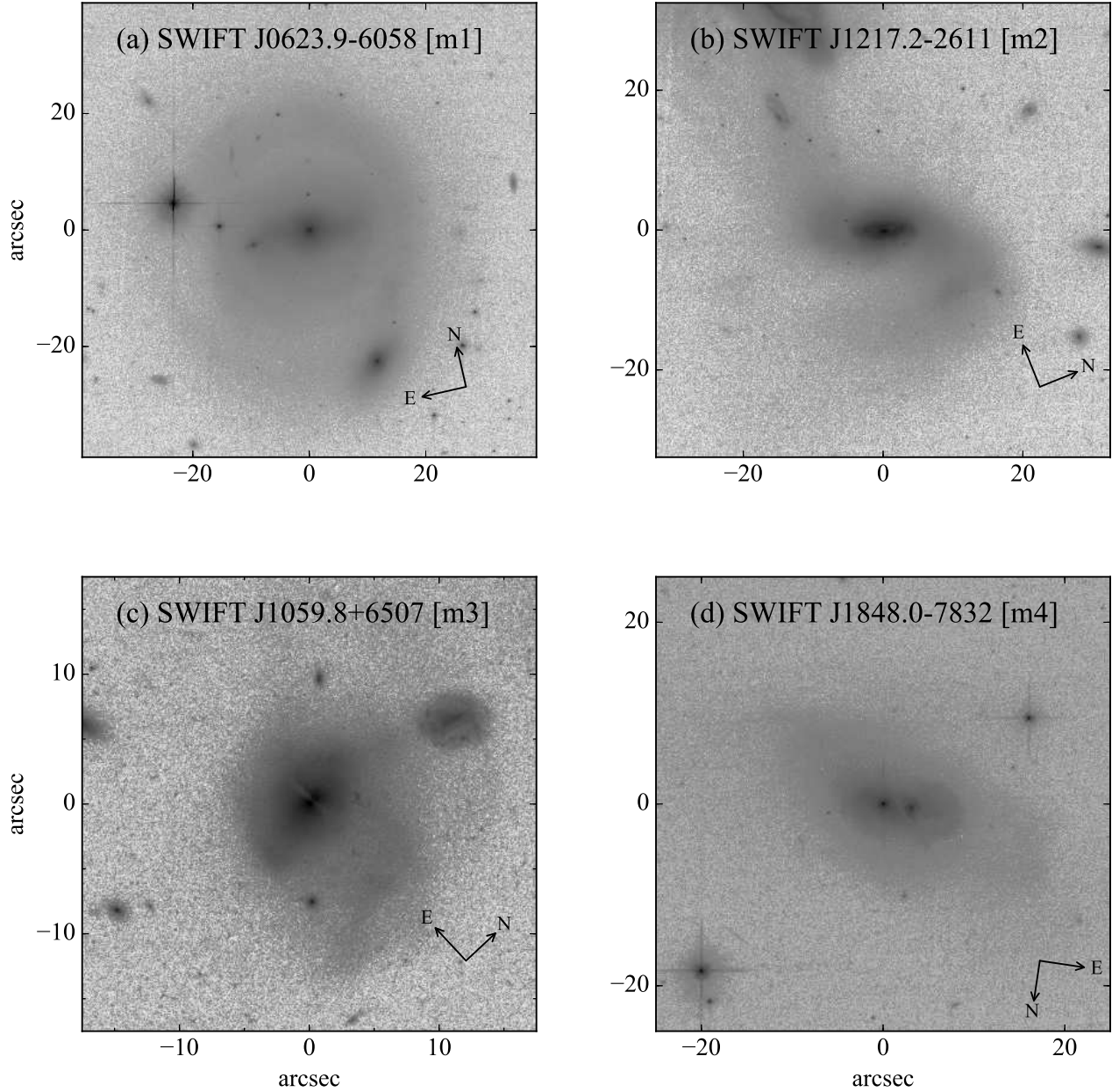


Figure 6. Example images of different subgroups based on their merging stages: (a) accompanying a galaxy with no (or weak) sign of interaction (m1); (b) merging galaxy without the major disturbance of the host (m2); (c) major disturbance but the companion galaxy is not yet merged (m3); (d) merging host with two galaxies sharing a common envelope (m4).

of their bulge and disk (Sa: bulge-dominated; Sb: intermediate bulge; Sc: disk-dominated). Where disagreement arises among the three classifiers, they reinspect the images until they reach convergence. The classifications of the sample are summarized in Table 2. The sample is roughly evenly divided between early-type hosts (74 or 48% E/S0) and late-type hosts (67 or 44% spi-

erals), with peculiar morphologies accounting for the minority (13 or 8%). Representative examples of each Hubble type are given in Figure 3.

Figure 4 shows the distributions of Hubble type as a function of bolometric luminosity and Eddington ratio. The ellipticals and peculiar galaxies appear to be found preferentially in more luminous AGN. However,

this trend is less significant in Eddington ratio. We also find that there is no substantial difference in the Hubble type distribution of type 1 versus type 2 AGN.

3.2. Signatures of Dynamical Perturbations

In addition to conventional morphological classification, we systematically search for the presence of irregular, asymmetric, features that are indicative of dynamical perturbations such as tidal interactions and galaxy-galaxy mergers. As with the main morphological classification, three co-authors visually examine the HST images based on four independent criteria. First, we divide the hosts into three groups depending on the presence of a tidal tail or shell. Second, hosts showing clear signs of interactions are identified, as either a “major merger” for the hosts that exhibit interacting companions of comparable brightness, or “minor merger” for those containing an apparent companion of significantly lower brightness. Third, by analogy with a similar classification scheme employed for luminous infrared galaxies (Haan et al. 2011; Stierwalt et al. 2013), we distinguish four merging stages: “m1” for hosts having a companion galaxy with no obvious signs of interaction; “m2” for hosts with signs of interaction, such as tidal tail or shell, but no major disturbances; “m3” for hosts with major disturbances but a companion galaxy that has not yet merged; and “m4” for hosts with two galaxies sharing a common envelope. And fourth, the hosts are split into three subgroups according to the presence of a double nucleus: “s” for hosts with a single nucleus; “d” for hosts with double nuclei residing in a single host; and “dd” for hosts with double nuclei in separate hosts.

The classifications based on the merging properties are listed in Table 2. Example images of different subtypes are displayed in Figure 5, and Figure 6 shows cutout images of hosts in different merging stages. We find 38 objects that are accompanied by tidal tails (27 objects) or shells (11 objects). Based on signs of interactions, 38 objects are classified as merging galaxies, among them 18 major mergers and 20 minor mergers. Intermediate and late merging stages (i.e. “m2”, “m3”, or “m4”) can be assigned to 28 objects. Note that this number of objects is slightly smaller than the values from other merging indicators (38) because the merging stage is defined only if the body of the companion galaxy is clearly seen in the science images. For example, a stellar stream or faint shell is not considered as a companion galaxy in this classification. Finally, only three objects appear to have double nuclei in a single host (i.e. “d”), while four objects have double nuclei in separate hosts (i.e. “dd”). We will discuss the physical connection between merging features and AGN properties in Section 5.2. The merg-

ing fraction as a function of different physical properties of AGN is summarized in Table 3.

4. DISCUSSION

4.1. Type 1 vs. Type 2

Because our sample is identified from Swift-BAT hard X-ray data and targets were selected for observation based on HST scheduling criteria unrelated to any galaxy properties other than location on the sky, selection biases resulting from X-ray obscuration or other AGN properties are minimized. Therefore, it should be possible to obtain a statistically meaningful comparison of the host properties of type 1 and type 2 AGN in this survey sample. We find that there is no significant difference in Hubble type between the hosts of the two types of AGN. Approximately 52, 41, and 7% of the type 1 targets and 44, 46, and 10% of type 2 targets are hosted by early-type, late-type, and peculiar galaxies, respectively. However, for the low-luminosity AGN ($L_{\text{bol}} \leq 10^{44.5} \text{ erg s}^{-1}$), the early-type fraction for type 2 ($\sim 48\%$) is marginally higher than that for type 1 ($\sim 37\%$). In other words, out of 35 early-type hosts for type 2 AGN, about half (18) contain low-luminosity AGN. On the contrary, out of 39 early-type hosts for type 1 AGN, only 18% (7) contain low-luminosity AGN. However, this luminosity dependence is not clearly detected in late-type hosts. We also confirm this trend using the Kolmogorov-Smirnov test to examine the distribution of bolometric luminosity of early-type hosts, finding that the null hypothesis that the two subsamples (type 1 and type 2) are drawn from the same population can be rejected with a confidence level of 99.9%.

It is worthwhile to note that the mean M_{BH} for type 2 AGN ($10^{8.20 \pm 0.58} M_{\odot}$) is marginally higher than that for type 1 AGN ($10^{8.04 \pm 0.78} M_{\odot}$) by ~ 0.2 dex. Therefore, the different levels of luminosity dependence of Hubble type between type 1 and type 2 AGN could originate from bias in the M_{BH} because galaxy morphology is a strong function of the stellar mass of the host. To test this hypothesis, we perform the same experiment using the subsample with M_{BH} ranging from $10^{7.5} M_{\odot}$ to $10^{9.5} M_{\odot}$, where the M_{BH} distributions of type 1 and type 2 AGN are similar. We again find that there are different levels of luminosity dependence between type 1 and type 2 AGN, indicating that such variation is not due to M_{BH} bias.

The merging properties in the host can also provide insight into the physical connection between type 1 and type 2 AGN. In this study, we consider hosts in relatively late stages (i.e. “m2”, “m3”, or “m4” in merging stages) as merging hosts. The merging fractions for both types of AGN are nearly identical (16% and 20%

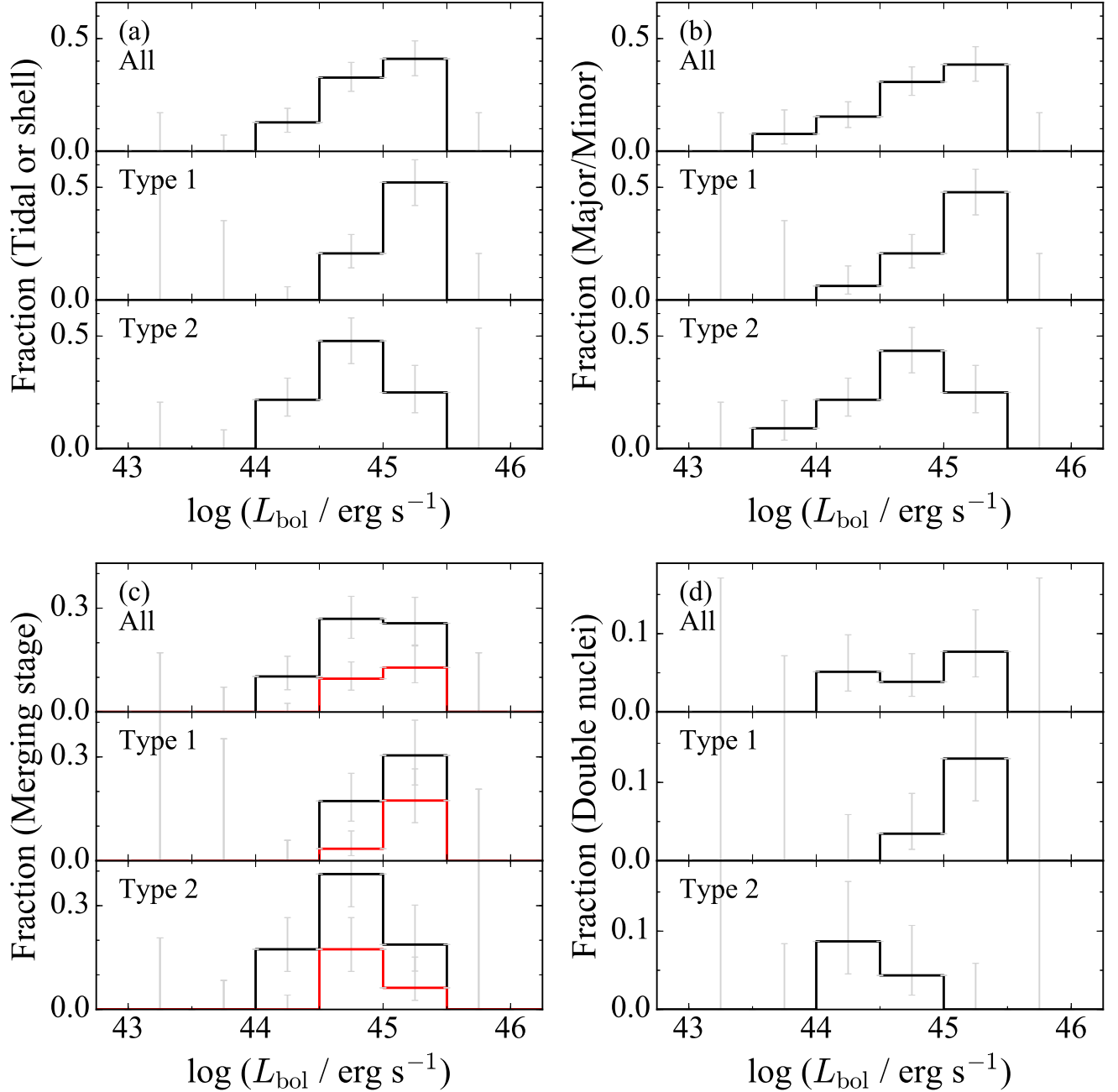


Figure 7. Dependence of the merging fraction on bolometric luminosity, for hosts with (a) a tidal tail or shell; (b) a major or minor merger; (c) tidal features that belong to merging stages “m2”, “m3”, or “m4” (black histograms) and those in the latest merging stages (“m4”; red histogram); (d) fraction of hosts having double nuclei (“d” or “dd”). Each panel shows separate distributions for all AGN, type 1 AGN, and type 2 AGN.

for type 1 and type 2, respectively). This is somewhat inconsistent with previous studies of nearby obscured AGN, which claimed that obscured AGN are more preferentially found in merging galaxies compared with unobscured AGN (e.g., Donley et al. 2018; Ellison et al. 2019). This discrepancy could be due to the fact that

IR-selected obscured AGN have higher merging fractions compared with optical and X-ray selected AGN.

We again divide the sample into two subgroups according to bolometric luminosity. For the low-luminosity AGN ($L_{\text{bol}} \leq 10^{44.5} \text{ erg s}^{-1}$), the merging fraction for

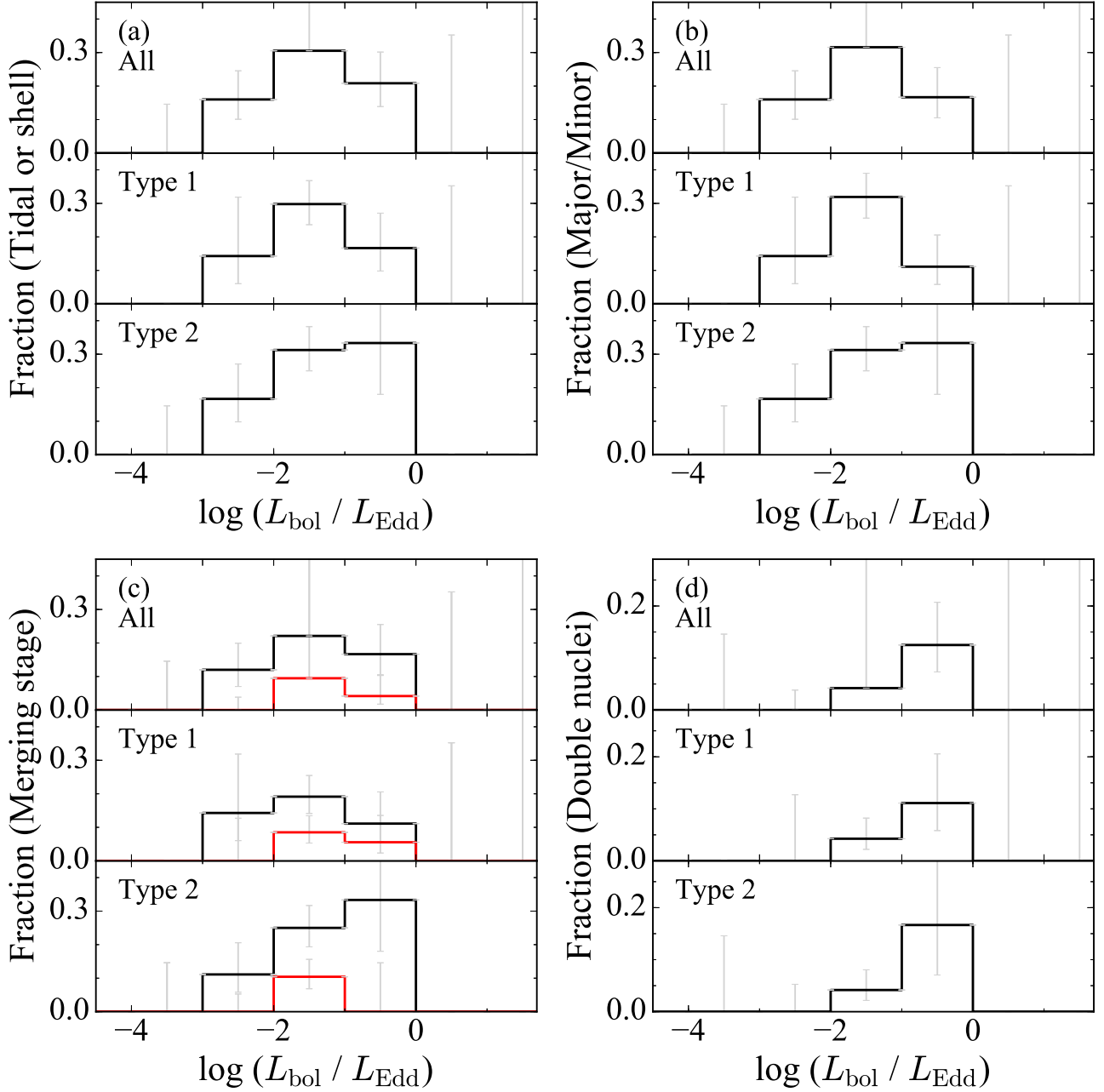


Figure 8. Dependence of the merging fraction on Eddington ratio, for hosts with (a) a tidal tail or shell; (b) a major or minor merger; (c) tidal features that belong to merging stages “m2”, “m3”, or “m4” (black histograms) and those in the latest merging stages (“m4”; red histogram); (d) fraction of hosts having double nuclei (“d” or “dd”). Each panel shows separate distributions for all AGN, type 1 AGN, and type 2 AGN.

type 2 ($11^{+5.5}_{-4.4}\%$ ⁴) is marginally higher than that for type 1 ($0^{+5.0}\%$). This luminosity dependence of the

⁴ Note that the error estimation in each bin is conducted using Jeffrey’s confidence interval, which is known to be robust for a small sample size.

merging fraction is also seen in Figure 7. This trend is commonly detected in various merging features (e.g., the existence of a tidal tail or shell, major or minor merging, and the presence of double nuclei; Figure 7). More interestingly, this discrepancy between type 1 and type 2 AGN disappears in the parameter space of Eddington ratio (Figure 8). Therefore, bolometric luminosity ap-

pears to be a main driver to determine the role merging plays in type 1 compared with type 2 AGN.

In addition, the merging fraction of type 1 AGN peaks at a higher bolometric luminosity compared with that of type 2 AGN. Taken at face value, this indicates either (1) the AGN triggering mechanism is not only dependent upon bolometric luminosity, but also differentiates somewhat between type 1 and type 2 AGN, or (2) the types are in different evolutionary stages, in the sense that type 2 precedes type 1.

4.2. Triggering Mechanism of AGN

The relative importance of internal (secular) and external (merger-driven) triggering of AGN is still not fully understood. While internal secular evolution in the host is thought to be responsible for enhancing the gas inflow toward a SMBH, for some AGN at least, galaxy merging is still regarded as a primary mechanism that triggers luminous AGN (e.g., [Hong et al. 2015](#); [Kim et al. 2017](#); [Marian et al. 2020](#)). The proximity of the target galaxies and deep HST images with high spatial resolution make our dataset useful to identify merging features. In this study, we compare visually identified merging features and physical properties of AGN to investigate the role merging plays in triggering AGN in the Swift-BAT sample.

We use four criteria to identify the merging features; merging fraction and its trend are in very good agreement with one another (Figs. 7 and 8). While these visual classifications are somewhat subjective and cannot capture the full complexity of galaxy mergers, we use these classifications as a simple proxy for the merger stage. Out of 154 targets, 28 ($\sim 18\%$) are classified as mergers (i.e., “m2”, “m3”, or “m4” in the merging stage). This is in good agreement with the result ($\sim 18\%$) derived using the SDSS images from a similar sample ([Koss et al. 2011](#)). [Zhao et al. \(2021\)](#) reached a similar conclusion from HST images of Palomar-Green QSOs at $z < 0.5$; they found that only 17% of the sample exhibits signs of interactions. However, our estimation of merging fraction is significantly lower than that for nearby luminous AGN ([Hong et al. 2015](#); [Gao et al. 2020](#); [Marian et al. 2020](#)). More strikingly, the merging fraction for less luminous AGN in our sample ($L_{\text{bol}} \leq 10^{44.5} \text{ erg s}^{-1}$) is dramatically lower than that for more luminous AGN ($L_{\text{bol}} > 10^{44.5} \text{ erg s}^{-1}$; $7.0^{+4.1}_{-2.6}\%$ versus $25^{+4.6}_{-4.12}\%$). Previous studies have shown that the merging fraction can be as high as $\sim 40 - 45\%$ for relatively nearby luminous AGN ($L_{\text{bol}} > 10^{45} \text{ erg s}^{-1}$). For example, [Hong et al. \(2015\)](#) claimed that the merger fraction of luminous AGN at $z < 0.3$ is $\sim 44\%$. [Marian et al. \(2020\)](#) analyzed ground-based optical images of lumi-

nous AGN at $z < 0.2$ and reached a similar conclusion (merging fraction of $\sim 41\%$). [Gao et al. \(2020\)](#) also showed that the merging fraction of less luminous AGN at $z < 0.1$ ($L_{\text{bol}} < 10^{45} \text{ erg s}^{-1}$) is as low as $\sim 20\%$ and that for more luminous AGN at $z < 0.6$ can be as high as $\sim 40\%$. Using more distant AGN ($z \sim 0.7$) but with moderate luminosity ($10^{42.5} < L_{\text{bol}} < 10^{45.5} \text{ erg s}^{-1}$), [Villforth et al. \(2014\)](#) found a merging fraction of $\sim 17\%$. For our sample, the merging fraction for $L_{\text{bol}} \leq 10^{45} \text{ erg s}^{-1}$ is $\sim 17\%$, and that for $L_{\text{bol}} > 10^{45} \text{ erg s}^{-1}$ is $\sim 23\%$. Therefore, our findings are in broad agreement with those of previous studies. However, the merging fraction for luminous AGN appears to be systematically lower than those from the literature. This discrepancy could be due to the fact that our $z < 0.1$ sample lacks highly luminous AGN ($L_{\text{bol}} > 10^{45.5} \text{ erg s}^{-1}$) that are better represented in more distant AGN samples.

As shown in Figure 7, the merging fraction dramatically increases as AGN luminosity increases. This trend is in good agreement with those of previous studies based on nearby and distant AGN ([Treister et al. 2012](#); [Kim et al. 2017](#); [Ellison et al. 2019](#)), suggesting that the luminous AGN are more likely to be triggered by merging. To the contrary, this tendency is not clearly observed in the comparison between the merging fraction and Eddington ratio (Figure 8). Taken at face value, the merging fraction also marginally increases as Eddington ratio increases. The merging fraction appears to peak at around $\log L_{\text{bol}}/L_{\text{Edd}} \sim -1.5$. This trend is more prominent for type 1 AGN although the significance of this finding should be further explored using larger sample sizes. It may also be related to the fact that NLS1, which tend to have large Eddington ratio, are preferentially found in non-merger barred hosts, revealing that lower mass BH can be efficiently fueled at a high rate through secular processes ([Crenshaw et al. 2003](#); [Orban de Xivry et al. 2011](#); [Kim et al. 2017](#)). Nevertheless, this finding suggests that merging may not be necessary to enhance the Eddington ratio (see also [Weigel et al. 2018](#)).

Using near-infrared (K -band) images obtained with adaptive optics for Swift-BAT AGN, [Koss et al. \(2018\)](#) claimed that luminous obscured AGN have an excess of late-stage mergers with double nuclei with a close separation ($d \leq 3 \text{ kpc}$) compared to unobscured AGN and inactive galaxies. Due to the high spatial resolution of the HST images, our dataset is suitable to test this finding independently, even though the obscuration tends to be more severe in I -band compared with K -band. In this study, we find only three objects (SWIFT J0234.6–0848,

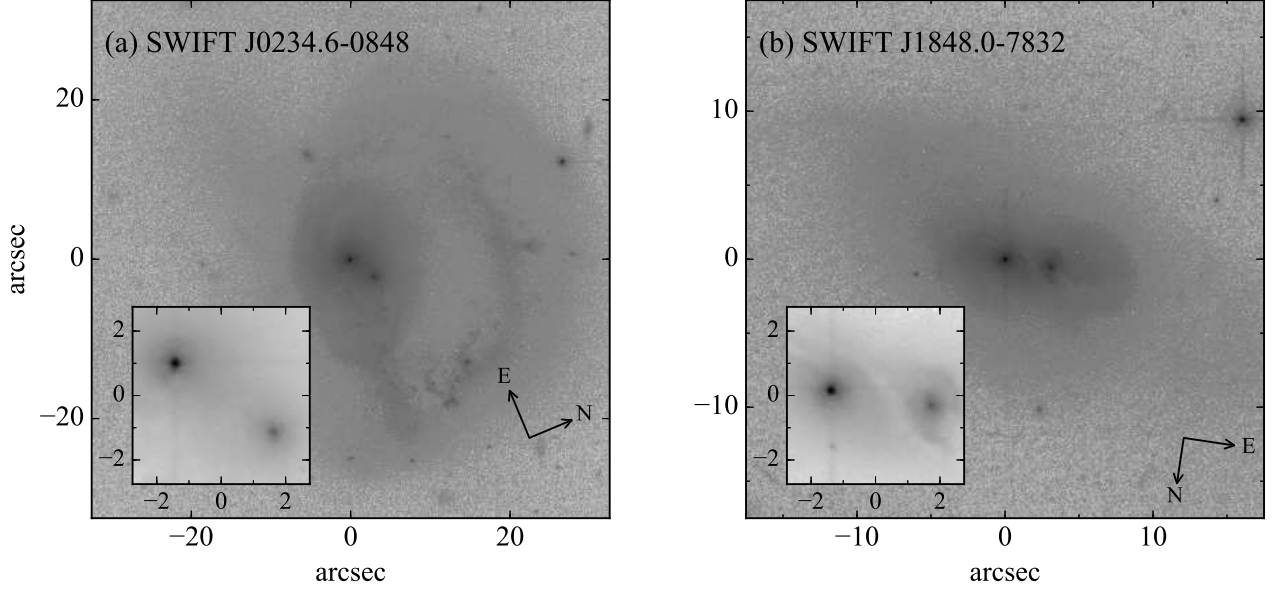


Figure 9. Double nuclei embedded in the host of (a) SWIFT J0234.6–0848 and (b) SWIFT J1848.0–7832. A close-up view of the central region is shown in the inset.

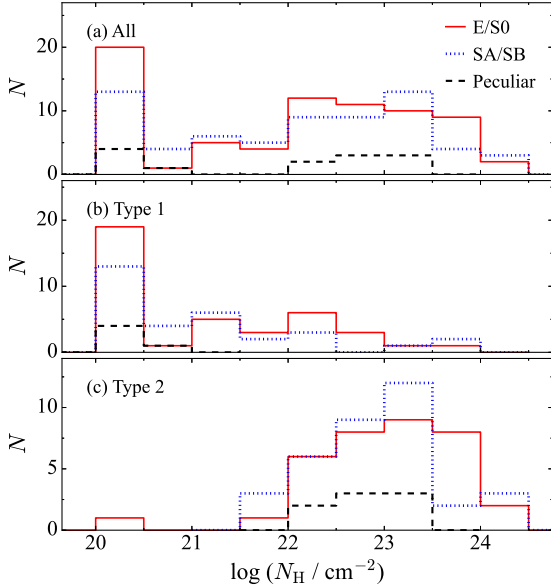


Figure 10. The distributions of the column density of neutral hydrogen (N_{H}) derived from X-ray observations (Ricci et al. 2017) for different morphological classifications. The red, blue, and black histograms denote early-type galaxies (E/S0), late-type galaxies with spiral arms (SA/SB), and peculiar galaxies, respectively.

SWIFT J1845.4+7211, and SWIFT J1848.0–7832; Figure 9) that have double nuclei in a single merged host (i.e., “d” in the number of nuclei). The separations between the two nuclei are $3''.7$ (2.6 kpc), $1''.6$ (1.5

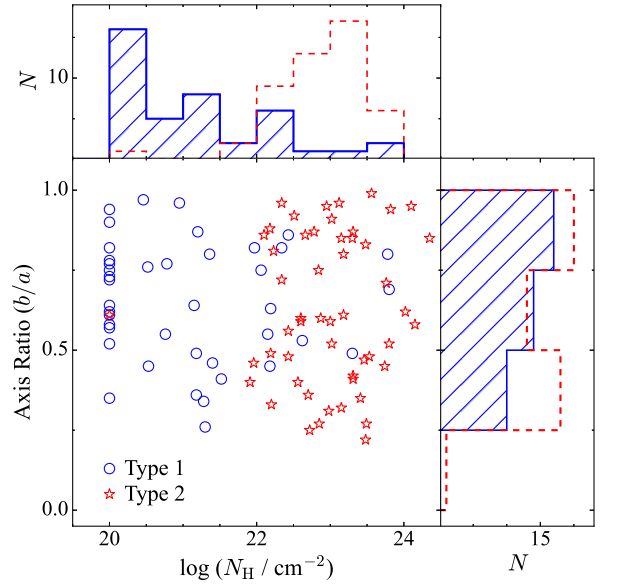


Figure 11. Distribution of host galaxy axis ratio (b/a) versus column density of neutral hydrogen (N_{H}) derived from X-ray observations (Ricci et al. 2017) for type 1 AGN (blue stars and blue histograms) and type 2 (red circles and red histograms) AGN.

kpc), and $3''.1$ (4.5 kpc) for SWIFT J0234.6–0848, SWIFT J1845.4+7211, and SWIFT J1848.0–7832, respectively. Thus, two objects from our survey (SWIFT J0234.6–0848 and SWIFT J1845.4+7211) sat-

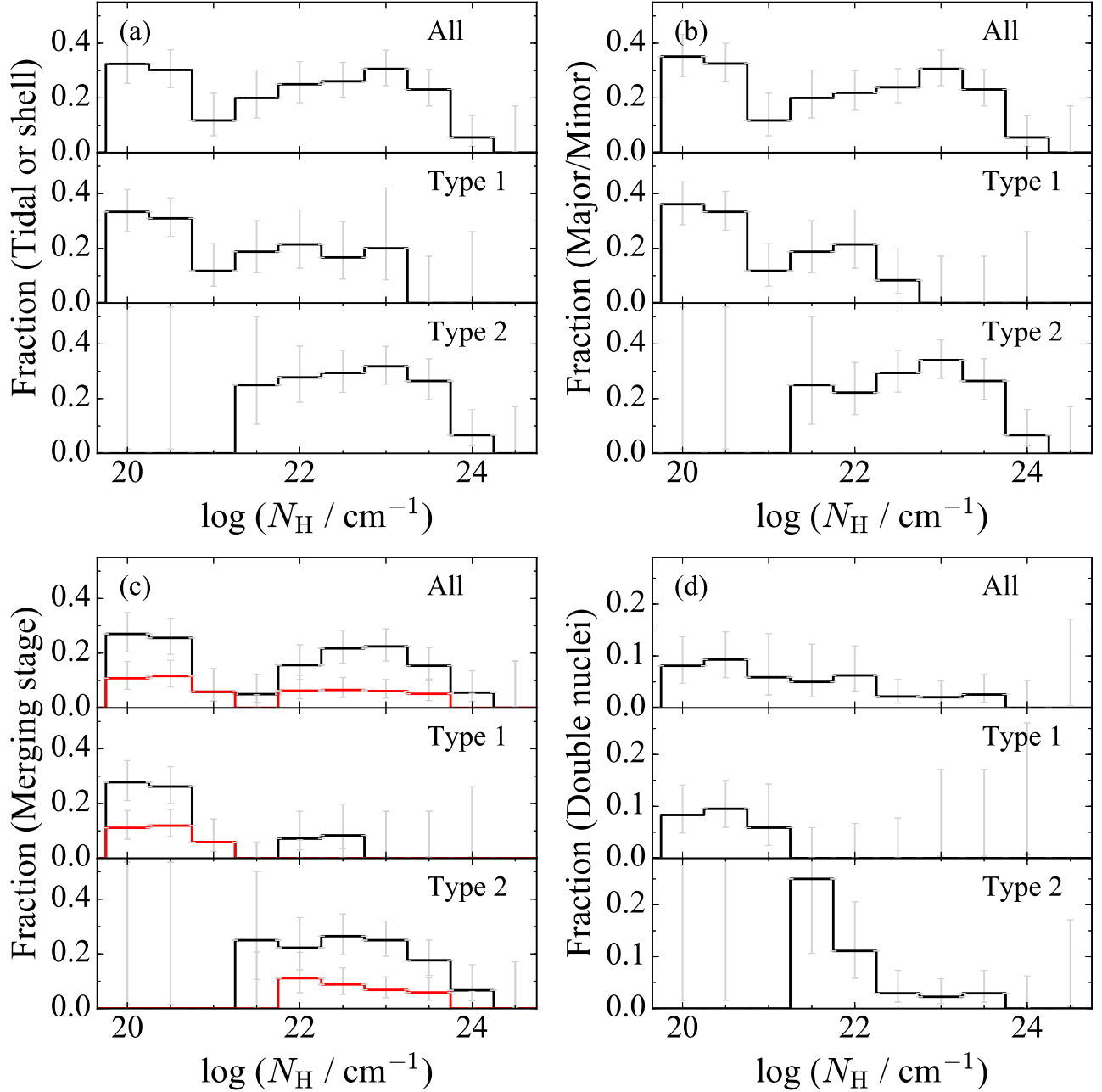


Figure 12. Dependence of the merging fraction on X-ray absorbing column density N_{H} , for hosts with (a) a tidal tail or shell; (b) a major or minor merger; (c) tidal features that belong to merging stages “m2”, “m3”, or “m4” (black histograms) and those in the latest merging stages (“m4”; red histogram); (d) fraction of hosts having double nuclei (“d” or “dd”). Each panel shows separate distributions for all AGN, type 1 AGN, and type 2 AGN. As described in the text, the fraction of galaxies found to contain double nuclei in this sample should be considered a lower limit, because the *I*-band imaging is not sufficient to identify some heavily obscured nuclei.

isfy the criteria ($d \leq 3$ kpc) for close-separation double nuclei from Koss et al. (2018). For comparison, two objects (SWIFT J0804.6+1045 and SWIFT J1845.4+7211) classified as close nuclei in Koss et al. (2018) are also observed in this study. While

SWIFT J1845.4+7211 is classified as “d” based on the nuclear structure visible in the HST F814W data, SWIFT J0804.6+1045 appears to have a single nucleus in the F814W image. This indicates that *I*-band images will miss some double nuclei that can be identified

in longer-wavelength imaging at comparable resolution, as would be expected for gas-rich mergers with highly obscured central regions.

Based on ground-based imaging surveys of nearby Swift-BAT AGN, several studies have independently examined the merging fraction using different methods (e.g., Koss et al. 2010, 2012; Cotini et al. 2013). For example, Koss et al. (2010) found that the fractions of disturbed host galaxies and of close pairs within 30 kpc in nearby sources ($z < 0.05$) are $\sim 18\%$ and $\sim 24\%$, respectively. The merging fraction coincides with our finding. The fraction of close pairs from this study ($\sim 33\%$) is marginally higher than that from Koss et al. (2010), although we do not impose any constraint on the distance to the companion, and the imaging quality of the two studies in terms of the depth and spatial resolution is not identical. Cotini et al. (2013) analyzed ground-based images of nearby sources ($z < 0.03$) to identify interacting systems through quantitative methods (Conselice 2003; Lotz et al. 2004). They found that the merging fraction is $20^{+7}_{-5}\%$, again in good agreement with this study. Finally, Koss et al. (2012) used optical spectroscopy and X-ray data to identify dual AGNs from the nearby Swift-BAT AGN ($z < 0.05$), and found that $\sim 10\%$ of the sample contains dual AGN. They also found that the fraction of dual AGN increases with increasing AGN luminosity, supporting the idea that merging plays an important role in luminous AGN.

4.3. Connection between the Obscuration and Merging Properties

As discussed in Section 5.1 and claimed in previous studies, there are marginal differences in the host properties between type 1 and type 2 AGN. Observational studies have found that significant obscuration can originate from dense material on larger scales in the host galaxy (e.g., Simcoe et al. 1997; Malkan et al. 1998; Malizia et al. 2020). In addition, theoretical and observational studies have suggested that the central BH can be heavily obscured during mergers (Sanders et al. 1988; Blecha et al. 2018). The hard X-ray selection makes the Swift-BAT sample particularly useful for exploring whether there is any connection between the degree of obscuration and the host galaxy morphological type or inclination. Here, we compare the hydrogen column density (N_H) as a proxy of obscuration with the host properties of our sample.

Figure 10 shows the distributions of column density for different morphologies. Based on the Kolmogorov–Smirnov test, there is no significant difference in N_H distributions between Hubble types. More surprisingly, the majority of highly obscured AGN

($\log N_H > 10^{23} \text{ cm}^{-2}$) are hosted by early-type galaxies. In addition, we compare the axis ratio with the hydrogen column density (Figure 11), and find there is no casual correlation between the two, and there is little difference in the axis ratio distributions between type 1 and type 2 AGN. These findings might indicate that the obscuration material is not physically related to the host galaxy, but rather to the nuclear torus.

We also compare the merging properties with N_H (Figure 12). As type 1 AGN tend to have a smaller N_H than type 2 by nature, it is not adequate to directly compare trends of type 1 and those of type 2 AGN. However, it is intriguing that the merging fractions appear to peak at $\log N_H \sim 10^{20} \text{ cm}^{-2}$ and $\log N_H \sim 10^{22-23} \text{ cm}^{-2}$. However, it is difficult to understand the origin of this bimodality; it might imply that the obscuration is somehow related to the various types of merging properties (e.g., gas contents, orbital motion, mass ratio, and merging stages). Contrary to our findings, previous observational studies claimed that obscured AGN, as opposed to unobscured AGN, are more likely to be hosted by galaxies that exhibit merging features (e.g., Urrutia et al. 2008; Kocevski et al. 2015). However, because previous studies primarily relied on red AGN selected from optical and IR bands (Glikman et al. 2015) or distant X-ray selected AGN ($z > 1$; Kocevski et al. 2015), the samples could be biased toward either luminous AGN or high- z environments, where merging plays a more important role in BH growth than at the present epoch.

5. SUMMARY

Through an intensive imaging survey of Swift-BAT AGN at $z < 0.1$ using the HST, we obtained coherent, deep I -band images for 154 targets. We conducted a visual classification of the host galaxies based on Hubble type and merging features. We also assembled AGN properties (BH mass, bolometric luminosity, Eddington ratio, and neutral hydrogen column density) of the sample from the literature, and compare them with the morphological properties of the hosts. From this program, we obtain the following results:

- Out of 154 targets, 74, 67, and 13 hosts are classified as early-type (E/S0), late-type (SA/SB) and peculiar galaxies, respectively.
- Using merger indicators including tidal tails and shells, we find 18%–25% of the sample is hosted by the merging galaxies, which is broadly consistent with the findings of previous studies. However, the merging fraction substantially is larger for high-luminosity AGN ($L_{\text{bol}} > 10^{44.5}$) compared with

less luminous AGN $L_{\text{bol}} \leq 10^{44.5}$ (25% versus 7%, respectively). It suggests that the merging plays a more important role in triggering luminous AGN in the Swift-BAT sample.

- To test AGN unification models, we compare the host morphologies of Type 1 and 2 AGN. We find there is a negligible difference in terms of Hubble type and merging fraction between these hosts. The merging fraction for Type 2 AGN, however, peaks at a marginally lower AGN luminosity than that of Type 1 AGN, implying that the triggering mechanism and/or evolutionary stage for Type 1 and Type 2 may differ somewhat.
- Finally, we compare the neutral hydrogen column density and axis ratio to host properties to investigate the origin of the obscuration. Although we did not identify any clear trend as a result of this comparison, we find that merging fractions appear to reach their maximum at $\log N_{\text{H}} \sim 10^{20} \text{ cm}^{-2}$ and $\log N_{\text{H}} \sim 10^{22-23}$. Although this bimodality has yet to be confirmed with a larger sample size, it could suggest that the physical origin of obscuration is complex.

The dataset presented in this paper will have broad applications for addressing other questions related to

the physical connection between SMBHs and their host galaxies. For example, we are currently performing two-dimensional imaging decomposition, and examining the $M_{\text{BH}} - L_{\text{bul}}$ relation for type 1 AGN. Our sample can also be combined with existing archival HST data of other Swift-BAT AGN, which will enable us to investigate the host galaxy statistical properties with a larger sample size. Finally, our extensive imaging survey can be used to carry out detailed host-galaxy studies of individual targets of interest among the nearby AGN population (e.g., Maksym et al. 2020).

ACKNOWLEDGMENTS

We are grateful to the anonymous referee for the constructive comments. We are grateful to STScI for supporting the gap-filler snapshot programs, and we thank Amber Armstrong and Norman Grogin for their assistance in preparing the Phase II program for this survey. LCH was supported by the National Science Foundation of China (11721303, 11991052, 12011540375) and the National Key R&D Program of China (2016YFA0400702). This work was supported by a National Research Foundation of Korea (NRF) grant (No. 2020R1A2C4001753) funded by the Korean government (MSIT) and under the framework of international cooperation program managed by the National Research Foundation of Korea (NRF-2020K2A9A2A06026245).

REFERENCES

- Antonucci, R. 1993, *ARA&A*, 31, 473
- Baumgartner, W. H., Tueller, J., Markwardt, C. B., et al. 2013, *ApJS*, 207, 19
- Bentz, M. C., Denney, K. D., Grier, C. J., et al. 2013, *ApJ*, 767, 149
- Bertin, E., & Arnouts, S. 1996, *A&AS*, 117, 393
- Bettoni, D., Falomo, R., Kotilainen, J. K., Karhunen, K., & Uslenghi, M. 2015, *MNRAS*, 454, 4103
- Blandford, R. D., & McKee, C. F. 1982, *ApJ*, 255, 419
- Blecha, L., Snyder, G. F., Satyapal, S., & Ellison, S. L. 2018, *MNRAS*, 478, 3056
- Böhm, A., Wisotzki, L., Bell, E. F., et al. 2013, *A&A*, 549, A46
- Canalizo, G., & Stockton, A. 2013, *ApJ*, 772, 132
- Chilingarian, I. V., Melchior, A.-L., & Zolotukhin, I. Y. 2010, *MNRAS*, 405, 1409
- Cisternas, M., Jahnke, K., Inskip, K. J., et al. 2011, *ApJ*, 726, 57
- Conselice, C. J. 2003, *ApJS*, 147, 1
- Cotini, S., Ripamonti, E., Caccianiga, A., et al. 2013, *MNRAS*, 431, 2661
- Crenshaw, D. M., Kraemer, S. B., & Gabel, J. R. 2003, *AJ*, 126, 1690
- Deo, R. P., Crenshaw, D. M., & Kraemer, S. B. 2006, *AJ*, 132, 321
- Di Matteo, T., Springel, V., & Hernquist, L. 2005, *Natur*, 433, 604
- Donley, J. L., Kartaltepe, J., Kocevski, D., et al. 2018, *ApJ*, 853, 63
- Du, P., Zhang, Z.-X., Wang, K., et al. 2018, *ApJ*, 856, 6
- Dunlop, J. S., McLure, R. J., Kukula, M. J., et al. 2003, *MNRAS*, 340, 1095
- Elitzur, M., Ho, L. C., & Trump, J. R. 2014, *MNRAS*, 438, 3340
- Ellison, S. L., Viswanathan, A., Patton, D. R., et al. 2019, *MNRAS*, 487, 2491
- Fabian, A. C. 1999, *MNRAS*, 308, L39
- Ferrarese, L., & Merritt, D. 2000, *ApJL*, 539, L9
- Fonseca Alvarez, G., Trump, J. R., Homayouni, Y., et al. 2020, *ApJ*, 899, 73
- Fukugita, M., Shimasaku, K., & Ichikawa, T. 1995, *PASP*, 107, 945

- Gao, F., Wang, L., Pearson, W. J., et al. 2020, *A&A*, 637, A94
- Gao, H., Ho, L. C., Barth, A. J., & Li, Z.-Y. 2019, *ApJS*, 244, 34
- Gebhardt, K., Bender, R., Bower, G., et al. 2000, *ApJL*, 539, L13
- Glikman, E., Simmons, B., Mailly, M., et al. 2015, *ApJ*, 806, 218
- Goulding, A. D., Greene, J. E., Bezanson, R., et al. 2018, *PASJ*, 70, S37
- Greene, J. E., & Ho, L. C. 2005, *ApJ*, 630, 122
- Greene, J. E., Strader, J., & Ho, L. C. 2020, *ARA&A*, 58, 257
- Greene, J. E., Peng, C. Y., Kim, M., et al. 2010, *ApJ*, 721, 26
- Grogin, N. A., Lim, P. L., Maybhate, A., Hook, R. N., & Loose, M. 2010, in *Hubble after SM4. Preparing JWST*, 54
- Grogin, N. A., Lim, P. L., Maybhate, A., Hook, R. N., & Loose, M. 2011, *Post-SM4 ACS/WFC Bias Striping: Characterization and Mitigation, Instrument Science Report ACS 2011-05*
- Haan, S., Surace, J. A., Armus, L., et al. 2011, *AJ*, 141, 100
- Ho, L. C., & Kim, M. 2014, *ApJ*, 789, 17
- . 2015, *ApJ*, 809, 123
- Hong, J., Im, M., Kim, M., & Ho, L. C. 2015, *ApJ*, 804, 34
- Hopkins, P. F., Hernquist, L., Cox, T. J., et al. 2005, *ApJ*, 630, 705
- Hopkins, P. F., Hernquist, L., Cox, T. J., & Kereš, D. 2008, *ApJS*, 175, 356
- Into, T., & Portinari, L. 2013, *MNRAS*, 430, 2715
- Ishibashi, W., & Fabian, A. C. 2016, *MNRAS*, 463, 1291
- Kaspi, S., Smith, P. S., Netzer, H., et al. 2000, *ApJ*, 533, 631
- Kim, M., & Ho, L. C. 2019, *ApJ*, 876, 35
- Kim, M., Ho, L. C., Peng, C. Y., Barth, A. J., & Im, M. 2017, *ApJS*, 232, 21
- Kim, M., Ho, L. C., Peng, C. Y., et al. 2008, *ApJ*, 687, 767
- Kocevski, D. D., Brightman, M., Nandra, K., et al. 2015, *ApJ*, 814, 104
- Kormendy, J., & Ho, L. C. 2013, *ARA&A*, 51, 511
- Koss, M., Mushotzky, R., Treister, E., et al. 2012, *ApJL*, 746, L22
- Koss, M., Mushotzky, R., Veilleux, S., & Winter, L. 2010, *ApJL*, 716, L125
- Koss, M., Mushotzky, R., Veilleux, S., et al. 2011, *ApJ*, 739, 57
- Koss, M., Trakhtenbrot, B., Ricci, C., et al. 2017, *ApJ*, 850, 74
- Koss, M. J., Blecha, L., Bernhard, P., et al. 2018, *Natur*, 563, 214
- Li, J. I. H., Shen, Y., Ho, L. C., et al. 2021, *ApJ*, 906, 103
- Lotz, J. M., Primack, J., & Madau, P. 2004, *AJ*, 128, 163
- Magorrian, J., Tremaine, S., Richstone, D., et al. 1998, *AJ*, 115, 2285
- Maksym, W. P., Schmidt, J., Keel, W. C., et al. 2020, *ApJL*, 902, L18
- Malizia, A., Bassani, L., Stephen, J. B., Bazzano, A., & Ubertini, P. 2020, *A&A*, 639, A5
- Malkan, M. A., Gorjian, V., & Tam, R. 1998, *ApJS*, 117, 25
- Marian, V., Jahnke, K., Andika, I., et al. 2020, *ApJ*, 904, 79
- Matsuoka, Y., Strauss, M. A., Price, III, T. N., & DiDonato, M. S. 2014, *ApJ*, 780, 162
- Nelson, C. H., MacKenty, J. W., Simkin, S. M., & Griffiths, R. E. 1996, *ApJ*, 466, 713
- Nolan, L. A., Dunlop, J. S., Kukula, M. J., et al. 2001, *MNRAS*, 323, 308
- Oh, K., Schawinski, K., Koss, M., et al. 2017, *MNRAS*, 464, 1466
- Orban de Xivry, G., Davies, R., Schartmann, M., et al. 2011, *MNRAS*, 417, 2721
- Park, D., Woo, J.-H., Bennert, V. N., et al. 2015, *ApJ*, 799, 164
- Planck Collaboration, Ade, P. A. R., Aghanim, N., et al. 2016, *A&A*, 594, A13
- Ricci, C., Trakhtenbrot, B., Koss, M. J., et al. 2017a, *ApJS*, 233, 17
- Ricci, C., Bauer, F. E., Treister, E., et al. 2017b, *MNRAS*, 468, 1273
- Sánchez, S. F., Jahnke, K., Wisotzki, L., et al. 2004, *ApJ*, 614, 586
- Sanders, D. B., Soifer, B. T., Elias, J. H., et al. 1988, *ApJ*, 325, 74
- Sani, E., Lutz, D., Risaliti, G., et al. 2010, *MNRAS*, 403, 1246
- Schade, D. J., Boyle, B. J., & Letawsky, M. 2000, *MNRAS*, 315, 498
- Schlafly, E. F., & Finkbeiner, D. P. 2011, *ApJ*, 737, 103
- Simcoe, R., McLeod, K. K., Schachter, J., & Elvis, M. 1997, *ApJ*, 489, 615
- Stierwalt, S., Armus, L., Surace, J. A., et al. 2013, *ApJS*, 206, 1
- Treister, E., Schawinski, K., Urry, C. M., & Simmons, B. D. 2012, *ApJL*, 758, L39
- Urrutia, T., Lacy, M., & Becker, R. H. 2008, *ApJ*, 674, 80
- Urry, C. M., & Padovani, P. 1995, *PASP*, 107, 803
- van Dokkum, P. G. 2001, *PASP*, 113, 1420
- Villforth, C., Hamann, F., Rosario, D. J., et al. 2014, *MNRAS*, 439, 3342

Villforth, C., Hamilton, T., Pawlik, M. M., et al. 2017,

MNRAS, 466, 812

Weigel, A. K., Schawinski, K., Treister, E., Trakhtenbrot,
B., & Sanders, D. B. 2018, MNRAS, 476, 2308
Zhao, D., Ho, L. C., Zhao, Y., Shangguan, J., & Kim, M.
2019, ApJ, 877, 52
Zhao, Y., Ho, L. C., Shangguan, J., et al. 2021, ApJ, 911, 94

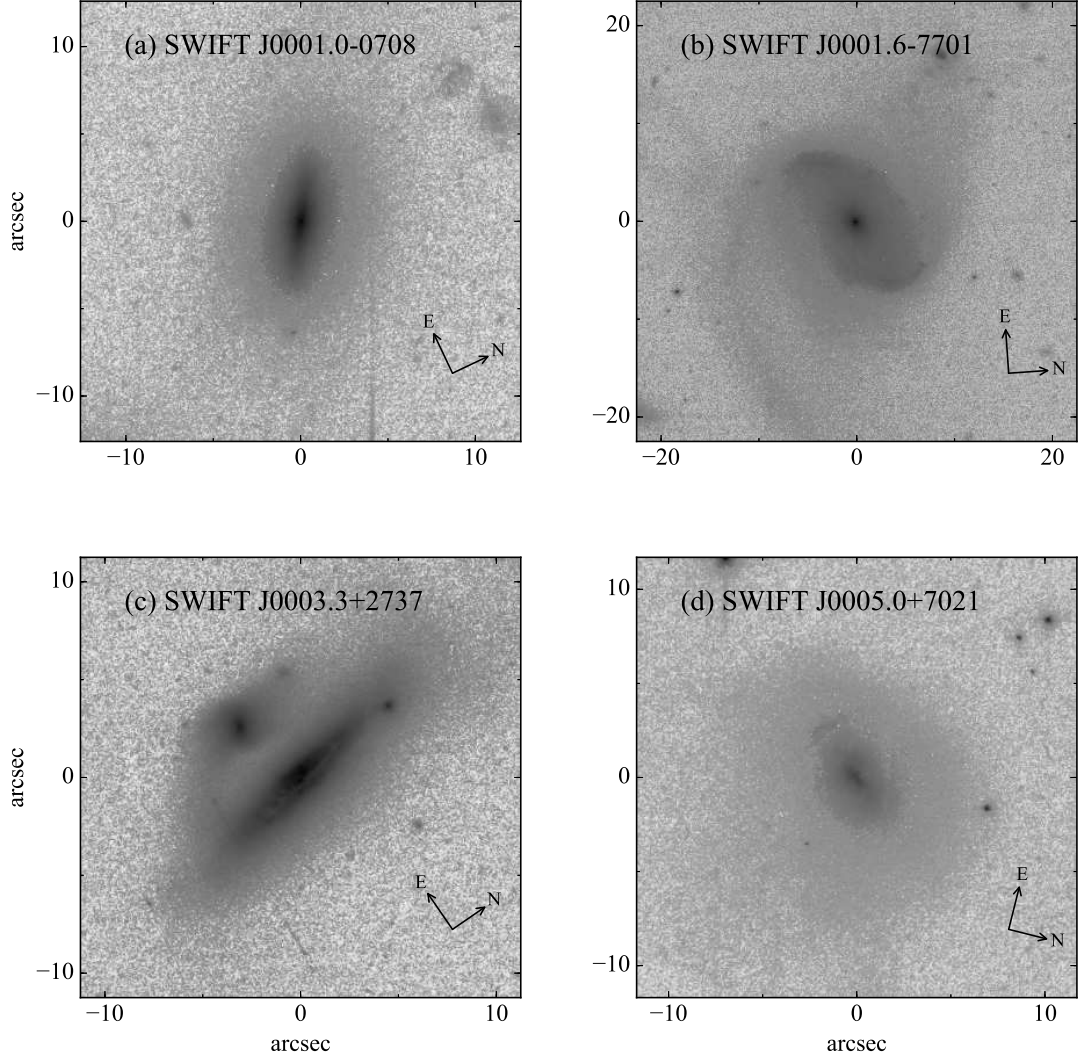


Figure 13. HST F814W-band images of the target galaxies. Images for the entire sample are available in the online figure set.

Fig. Set 13. Images

Table 1. The sample

Source Name	Alt. Name	R.A.	Dec.	A_V	z	Type	Obs. Date	$\log L_{\text{bol}}$	$\log M_{\text{BH}}$	M	$\log \lambda$	b/a	$\log N_{\text{H}}$
		(deg.)	(deg.)	(mag)				(erg s ⁻¹)	(M_{\odot})				(cm ⁻²)
(1)	(2)	(3)	(4)	(5)	(6)	(7)	(8)	(9)	(10)	(11)	(12)	(13)	(14)
SWIFT J0001.0–0708		0.2032	-7.1532	0.087	0.0375	1	2018-12-05	44.50	7.12	H α	-0.72	0.63	22.19 ^{+0.07} _{-0.08}
SWIFT J0001.6–7701	Fairall 1203	0.4419	-76.9540	0.160	0.0585	1	2018-12-23	44.82	8.75	M_*	-2.03	0.90	20.00 ^{+0.00} _{-0.00}
SWIFT J0003.3+2737		0.8643	27.6548	0.164	0.0397	2	2019-01-22	44.57	7.85	σ_*	-1.38	0.37	22.86 ^{+0.12} _{-0.08}
SWIFT J0005.0+7021		1.0082	70.3217	2.313	0.0964	1	2018-12-02	45.33	8.20	M_*	-0.97	0.87	22.61 ^{+0.07} _{-0.05}
SWIFT J0006.2+2012	Mrk 335	1.5813	20.2029	0.096	0.0259	1	2018-05-20	44.30	7.34	H α	-1.14	0.87	20.48 ^{+0.03} _{-0.22}
SWIFT J0036.3+4540		9.0874	45.6650	0.181	0.0476	1	2019-01-12	44.80	8.54	M_*	-1.84	0.52	20.00 ^{+0.00} _{-0.00}
SWIFT J0100.9–4750	ESO 195-IG 021 NED03	15.1457	-47.8676	0.037	0.0484	2	2018-03-31	44.84	8.42	σ_*	-1.68	0.39	22.57 ^{+0.03} _{-0.04}
SWIFT J0123.9–5846	Fairall 9	20.9408	-58.8057	0.071	0.0460	1	2018-12-25	45.32	8.38	H α	-1.16	0.85	20.00 ^{+0.00} _{-0.00}
SWIFT J0128.4+1631	CGCG 459-058	22.1017	16.4593	0.199	0.0387	1	2019-01-22	44.57	6.51	H α	-0.04	0.49	23.30 ^{+0.18} _{-0.04}
SWIFT J0134.1–3625	NGC 612	23.4906	-36.4933	0.055	0.0298	2	2018-12-25	45.23	8.99	σ_*	-1.86	0.86	23.97 ^{+0.11} _{-0.07}
SWIFT J0157.2+4715		29.2956	47.2666	0.409	0.0478	1	2019-01-13	44.84	7.85	H α	-1.11	0.82	20.00 ^{+0.00} _{-0.00}
SWIFT J0202.4+6824A		30.5720	68.3620	3.094	0.0119	2	2019-01-20	43.38	8.94	M_*	-3.66	0.81	22.23 ^{+0.35} _{-0.45}
SWIFT J0202.4+6824B		30.3850	68.4061	3.085	0.0152	2	2019-01-20	43.50	9.04	M_*	-3.64	0.86	22.10 ^{+0.13} _{-0.69}
SWIFT J0206.2–0019	Mrk 1018	31.5666	-0.2914	0.075	0.0430	1	2019-01-11	45.01	8.00	H α	-1.09	0.64	20.00 ^{+0.00} _{-0.00}
SWIFT J0234.6–0848	NGC 985	38.6574	-8.7876	0.090	0.0430	1	2019-01-16	45.02	8.43	H α	-1.51	0.93	20.92 ^{+0.09} _{-0.06}
SWIFT J0243.9+5324	2MFGC 02171	41.0125	53.4745	1.040	0.0364	2	2019-01-12	44.29	7.83	M_*	-1.64	0.25	22.72 ^{+0.17} _{-0.12}
SWIFT J0333.3+3720		53.3282	37.3030	1.465	0.0547	1	2019-01-11	45.14	8.15	H α	-1.11	0.80	21.36 ^{+0.16} _{-0.20}
SWIFT J0347.0–3027		56.7729	-30.3972	0.030	0.0950	1	2018-12-21	45.18	7.76	M_*	-0.68	0.72	20.00 ^{+0.00} _{-0.00}
SWIFT J0356.9–4041		59.2356	-40.6960	0.023	0.0747	2	2018-12-19	45.22	8.74	M_*	-1.62	0.86	22.66 ^{+0.03} _{-0.04}
SWIFT J0405.3–3707	ESO 359- G 019	61.2570	-37.1875	0.016	0.0552	1	2019-01-13	44.77	8.18	M_*	-1.51	0.61	20.00 ^{+0.00} _{-0.00}
SWIFT J0429.6–2114		67.4095	-21.1622	0.067	0.0700	1	2018-11-26	45.00	8.72	H α	-1.82	0.70	20.00 ^{+0.00} _{-0.00}
SWIFT J0443.9+2856		70.9450	28.9718	2.028	0.0217	1	2018-11-13	44.48	8.08	M_*	-1.70	0.82	22.34 ^{+0.03} _{-0.03}
SWIFT J0446.4+1828	UGC 3157	71.6240	18.4609	1.646	0.0158	1	2019-01-21	43.91	6.69	H α	-0.88	0.80	23.78 ^{+0.21} _{-0.19}
SWIFT J0456.3–7532	ESO 033- G 002	73.9957	-75.5412	0.400	0.0181	2	2018-12-14	44.13	8.44	M_*	-2.41	0.92	22.51 ^{+0.40} _{-0.31}
SWIFT J0504.6–7345		76.1425	-73.8242	0.335	0.0451	2	2020-10-02	44.52	8.58	M_*	-2.16	0.40	21.91 ^{+0.14} _{-0.14}
SWIFT J0510.7+1629	IRAS 05078+1626	77.6896	16.4989	0.820	0.0173	1	2019-01-19	44.72	7.64	H α	-1.02	0.66	21.08 ^{+0.07} _{-0.10}
SWIFT J0516.2–0009	Ark 120	79.0476	-0.1498	0.349	0.0325	1	2018-11-28	45.11	8.68	H α	-1.67	0.82	20.00 ^{+0.00} _{-0.00}
SWIFT J0526.2–2118	ESO 553- G 043	81.6135	-21.2866	0.116	0.0277	2	2019-01-22	44.30	8.05	σ_*	-1.85	0.85	23.30 ^{+0.07} _{-0.07}
SWIFT J0528.1–3933		82.0086	-39.5791	0.073	0.0369	2	2020-05-31	44.37	8.20	M_*	-1.93	0.49	21.68 ^{+0.22} _{-0.28}
SWIFT J0533.9–1318		83.4589	-13.3553	0.371	0.0290	2	2019-10-23	44.52	8.51	M_*	-2.09	0.71	23.76 ^{+0.19} _{-0.33}

Table 1 *continued*

Table 1 (continued)

Source Name	Alt. Name	R.A.	Dec.	A_V	z	Type	Obs. Date	$\log L_{\text{bol}}$	$\log M_{\text{BH}}$	M	$\log \lambda$	b/a	$\log N_{\text{H}}$
		(deg.)	(deg.)	(mag)				(erg s^{-1})	(M_{\odot})				(cm^{-2})
(1)	(2)	(3)	(4)	(5)	(6)	(7)	(8)	(9)	(10)	(11)	(12)	(13)	(14)
SWIFT J0544.4–4328		86.0000	-43.4240	0.132	0.0446	2	2021-04-07	44.45	7.40	M_*	-1.05	0.46	$22.81^{+0.14}_{-0.19}$
SWIFT J0552.5+5929		88.1169	59.4756	0.511	0.0585	1	2018-11-19	44.96	8.35	M_*	-1.49	0.82	$20.00^{+0.00}_{-0.00}$
SWIFT J0623.9–6058	ESO 121-IG 028	95.9400	-60.9790	0.158	0.0405	2	2018-12-14	44.98	9.04	M_*	-2.16	0.87	$23.31^{+0.05}_{-0.04}$
SWIFT J0641.3+3257		100.3252	32.8254	0.414	0.0486	2	2018-12-22	45.15	8.12	σ_*	-1.07	0.96	$23.12^{+0.05}_{-0.06}$
SWIFT J0645.9+5303		101.6108	53.0758	0.207	0.0359	2	2020-04-14	44.41	8.06	M_*	-1.75	0.96	$22.34^{+0.16}_{-0.15}$
SWIFT J0707.1+6433		106.8047	64.5997	0.104	0.0797	1	2019-01-16	45.10	8.56	M_*	-1.56	0.90	$20.00^{+0.00}_{-0.00}$
SWIFT J0709.0–4642		107.1803	-46.7137	0.298	0.0468	2	2018-12-22	44.74	8.25	σ_*	-1.61	0.66	$22.40^{+0.16}_{-0.12}$
SWIFT J0736.9+5846	Mrk 9	114.2374	58.7704	0.160	0.0399	1	2019-01-11	44.40	7.84	H α	-1.54	0.97	$20.46^{+0.28}_{-0.31}$
SWIFT J0743.0+6513	Mrk 78	115.6739	65.1771	0.097	0.0366	2	2019-01-06	44.49	8.27	M_*	-1.88	0.58	$24.15^{+0.11}_{-0.13}$
SWIFT J0743.3–2546		115.8114	-25.7639	1.969	0.0238	1	2018-12-17	44.30	7.39	H α	-1.19	0.96	$20.95^{+0.25}_{-1.65}$
SWIFT J0747.5+6057	Mrk 10	116.8714	60.9335	0.128	0.0294	1	2019-01-10	44.36	7.54	H α	-1.28	0.45	$20.53^{+0.22}_{-0.12}$
SWIFT J0747.6–7326		116.9098	-73.4314	1.128	0.0359	2	2019-12-27	44.61	8.84	M_*	-2.33	0.99	$23.56^{+0.19}_{-0.16}$
SWIFT J0753.1+4559	B3 0749+460A	118.1842	45.9493	0.226	0.0516	1	2019-01-08	44.83	8.38	H α	-1.65	0.94	$20.00^{+0.00}_{-0.00}$
SWIFT J0756.3–4137		119.0817	-41.6284	2.116	0.0210	2	2019-01-16	43.90	6.94	H α	-1.14	0.56	$21.77^{+0.07}_{-0.07}$
SWIFT J0759.8–3844		119.9242	-38.7322	2.225	0.0402	1	2019-02-03	45.15	8.52	H α	-1.47	0.73	$20.00^{+0.00}_{-0.00}$
SWIFT J0800.1+2638	IC 0486	120.0874	26.6135	0.111	0.0266	1	2018-12-29	44.59	7.06	H α	-0.57	0.75	$22.06^{+0.12}_{-0.11}$
SWIFT J0801.9–4946		120.4915	-49.7784	0.709	0.0405	1	2020-05-11	44.80	9.23	M_*	-2.53	0.36	$21.18^{+0.14}_{-0.18}$
SWIFT J0804.6+1045	MCG +02-21-013	121.1933	10.7767	0.073	0.0349	2	2018-12-28	44.55	8.21	σ_*	-1.76	0.41	$23.02^{+0.15}_{-0.22}$
SWIFT J0805.1–0110		121.2208	-1.1466	0.071	0.0915	2	2021-03-26	45.39	8.45	σ_*	-1.16	0.47	$23.46^{+0.16}_{-0.31}$
SWIFT J0807.9+3859	Mrk 622	121.9210	39.0042	0.138	0.0232	2	2018-05-25	44.32	6.74	H α	-0.52	0.95	$24.10^{+1.90}_{-0.43}$
SWIFT J0819.2–2259		124.7410	-22.8770	0.335	0.0346	1	2020-05-03	44.39	8.31	M_*	-2.02	0.75	$20.00^{+0.00}_{-0.00}$
SWIFT J0823.4–0457	Fairall 272	125.7546	-4.9349	0.125	0.0222	2	2018-04-08	44.66	8.14	σ_*	-1.58	0.48	$23.53^{+0.05}_{-0.04}$
SWIFT J0840.2+2947	4C +29.30	130.0099	29.8174	0.153	0.0647	2	2019-01-21	45.28	8.77	σ_*	-1.59	0.85	$23.80^{+0.11}_{-0.10}$
SWIFT J0855.6+6425	MCG +11-11-032	133.8023	64.3959	0.279	0.0362	2	2019-01-05	44.66	8.35	σ_*	-1.79	0.42	$23.31^{+0.13}_{-0.13}$
SWIFT J0902.7–4814		135.6555	-48.2261	4.222	0.0391	1	2020-07-31	44.90	5.54	M_*	1.26	0.77	$22.15^{+0.13}_{-0.22}$
SWIFT J0923.7+2255	MCG +04-22-042	140.9292	22.9090	0.120	0.0333	1	2019-01-11	44.87	7.54	H α	-0.77	0.57	$20.00^{+0.00}_{-0.00}$
SWIFT J0924.2–3141		140.9739	-31.6919	0.408	0.0426	2	2020-04-27	45.00	8.05	M_*	-1.15	0.75	$24.42^{+0.09}_{-0.07}$
SWIFT J0925.2–8423		141.5735	-84.3593	0.540	0.0629	1	2018-12-28	44.85	7.81	M_*	-1.06	0.78	$22.40^{+0.08}_{-0.12}$
SWIFT J0936.2–6553		144.0260	-65.8093	0.640	0.0393	2	2018-12-25	44.50	7.97	M_*	-1.57	0.59	$22.60^{+0.35}_{-2.60}$
SWIFT J0942.2+2344	CGCG 122-055	145.5200	23.6853	0.069	0.0217	1	2019-01-19	43.98	7.35	H α	-1.47	0.77	$20.78^{+0.33}_{-1.22}$
SWIFT J0947.6–3057	MCG -05-23-016	146.9173	-30.9489	0.295	0.0083	1	2019-01-23	44.40	6.62	H α	-0.32	0.45	$22.18^{+0.03}_{-0.04}$
SWIFT J1020.5–0237B		154.9941	-2.5767	0.112	0.0595	1	2019-01-19	44.60	8.58	H β	-2.08	0.94	$20.00^{+0.00}_{-0.00}$

Table 1 continued

Table 1 (*continued*)

Source Name	Alt. Name	R.A.	Dec.	A_V	z	Type	Obs. Date	$\log L_{\text{bol}}$	$\log M_{\text{BH}}$	M	$\log \lambda$	b/a	$\log N_{\text{H}}$
		(deg.)	(deg.)	(mag)				(erg s^{-1})	(M_{\odot})				(cm^{-2})
(1)	(2)	(3)	(4)	(5)	(6)	(7)	(8)	(9)	(10)	(11)	(12)	(13)	(14)
SWIFT J1021.7–0327	ARK 241	155.4177	-3.4539	0.123	0.0410	1	2019-01-17	44.72	8.15	M_*	-1.53	0.89	$20.00^{+0.00}_{-0.00}$
SWIFT J1029.8–3821	ESO 317- G 038	157.4400	-38.3486	0.199	0.0151	2	2021-05-11	43.65	7.41	σ_*	-1.86	0.35	$23.41^{+0.42}_{-0.30}$
SWIFT J1031.9–1418		157.9763	-14.2809	0.183	0.0851	1	2019-10-30	45.67	8.73	H α	-1.16	0.93	$20.00^{+0.00}_{-0.00}$
SWIFT J1032.7–2835	ESO 436- G 034	158.1855	-28.6101	0.170	0.0121	2	2021-03-12	43.60	8.07	σ_*	-2.57	0.27	$22.85^{+0.21}_{-0.14}$
SWIFT J1033.6+7303	CGCG 333-038	158.5981	73.0140	0.343	0.0224	1	2021-03-12	44.06	8.01	M_*	-2.05	0.53	$22.62^{+0.17}_{-0.21}$
SWIFT J1038.8–4942		159.6883	-49.7816	1.360	0.0602	1	2021-03-12	45.15	8.56	H β	-1.51	0.80	$22.73^{+0.05}_{-0.05}$
SWIFT J1040.7–4619		160.0939	-46.4238	0.424	0.0238	2	2019-01-16	44.21	8.52	σ_*	-2.41	0.60	$22.60^{+0.03}_{-0.02}$
SWIFT J1042.4+0046		160.5349	0.7017	0.153	0.0952	2	2021-03-12	45.30	7.89	M_*	-0.69	0.33	$22.20^{+0.14}_{-0.12}$
SWIFT J1043.4+1105	SDSS J104326.47+110524.2	160.8603	11.0901	0.075	0.0480	1	2021-03-12	44.73	8.29	H α	-1.66	0.85	$20.00^{+0.00}_{-0.00}$
SWIFT J1059.8+6507		164.9315	65.0684	0.070	0.0835	2	2018-07-30	45.16	8.45	σ_*	-1.39	0.79	$22.53^{+0.10}_{-0.10}$
SWIFT J1132.9+1019A	IC 2921	173.2053	10.2965	0.090	0.0440	1	2019-01-22	44.72	7.84	H α	-1.22	0.41	$21.52^{+0.23}_{-0.22}$
SWIFT J1136.7–6007		174.1752	-60.0519	2.599	0.0142	2	2019-01-25	43.87	7.92	M_*	-2.15	0.48	$22.43^{+0.15}_{-0.20}$
SWIFT J1139.1+5913	SBS 1136+594	174.7870	59.1990	0.041	0.0616	1	2018-03-28	45.14	8.21	H α	-1.17	0.53	$20.00^{+0.00}_{-0.00}$
SWIFT J1143.7+7942	UGC 06728	176.3168	79.6815	0.278	0.0063	1	2020-03-02	43.28	6.01	H α	-0.83	0.78	$20.00^{+0.00}_{-0.00}$
SWIFT J1148.3+0901		176.9795	9.0413	0.074	0.0693	1	2019-01-10	45.02	8.63	H α	-1.71	0.62	$20.00^{+0.00}_{-0.00}$
SWIFT J1200.2–5350		180.6985	-53.8355	0.562	0.0277	2	2020-09-02	44.81	7.98	σ_*	-1.27	0.52	$22.46^{+0.02}_{-0.03}$
SWIFT J1211.3–3935		182.8095	-39.5574	0.233	0.0609	2	2019-01-11	45.16	8.57	σ_*	-1.51	0.49	$22.19^{+0.06}_{-0.08}$
SWIFT J1213.1+3239A	CGCG 187-022	183.2888	32.5964	0.034	0.0248	2	2018-12-17	44.18	7.75	σ_*	-1.67	0.45	$23.74^{+0.29}_{-0.46}$
SWIFT J1217.2–2611	ESO 505-IG 030	184.2380	-26.2093	0.224	0.0393	2	2020-04-24	44.60	7.79	M_*	-1.29	0.26	$23.28^{+0.06}_{-0.20}$
SWIFT J1248.2–5828		191.9910	-58.5001	1.649	0.0279	2	2020-07-15	44.08	8.03	M_*	-2.05	0.34	$22.46^{+0.23}_{-0.20}$
SWIFT J1306.4–4025B		196.8004	-40.4076	0.280	0.0159	2	2019-01-13	43.79	7.68	M_*	-1.99	0.61	$20.00^{+0.00}_{-0.00}$
SWIFT J1315.8+4420	UGC 08327 NED02	198.8220	44.4071	0.052	0.0355	2	2018-04-23	44.63	8.67	σ_*	-2.14	0.69	$22.88^{+0.07}_{-0.05}$
SWIFT J1316.9–7155		199.2262	-71.9242	0.699	0.0703	1	2018-12-26	45.16	9.03	H β	-1.97	0.86	$20.00^{+0.00}_{-0.00}$
SWIFT J1322.2–1641	MCG -03-34-064	200.6019	-16.7286	0.215	0.0168	1	2019-01-18	44.32	7.14	H α	-0.92	0.69	$23.80^{+0.02}_{-0.02}$
SWIFT J1332.0–7754		203.1692	-77.8446	0.577	0.0098	2	2020-03-30	43.60	8.78	M_*	-3.28	0.52	$23.80^{+0.12}_{-0.08}$
SWIFT J1333.5–3401	ESO 383-18	203.3587	-34.0148	0.163	0.0128	2	2020-04-13	43.85	6.94	M_*	-1.19	0.41	$23.31^{+0.03}_{-0.02}$
SWIFT J1336.0+0304	NGC 5231	203.9510	2.9990	0.066	0.0216	2	2019-01-13	44.06	7.95	σ_*	-1.99	0.72	$22.34^{+0.04}_{-0.02}$
SWIFT J1338.2+0433	NGC 5252	204.5665	4.5426	0.095	0.0229	2	2018-06-18	45.00	8.87	σ_*	-1.97	0.56	$22.43^{+0.02}_{-0.02}$
SWIFT J1341.5+6742	NGC 5283	205.2740	67.6723	0.052	0.0103	2	2019-10-26	43.23	8.87	σ_*	-3.74	0.85	$23.15^{+0.08}_{-0.10}$
SWIFT J1345.5+4139	NGC 5290	206.3299	41.7126	0.019	0.0085	2	2018-07-19	43.36	7.76	σ_*	-2.50	0.46	$21.96^{+0.08}_{-0.06}$
SWIFT J1349.7+0209	UM 614	207.4701	2.0791	0.077	0.0331	1	2019-01-03	44.51	7.50	H α	-1.09	0.49	$21.18^{+0.10}_{-0.07}$
SWIFT J1354.5+1326		208.6211	13.4659	0.077	0.0633	2	2019-01-15	44.89	7.74	M_*	-0.95	0.38	$23.34^{+0.12}_{-0.09}$

Table 1 *continued*

Table 1 (continued)

Source Name	Alt. Name	R.A.	Dec.	A_V	z	Type	Obs. Date	$\log L_{\text{bol}}$	$\log M_{\text{BH}}$	M	$\log \lambda$	b/a	$\log N_{\text{H}}$
		(deg.)	(deg.)	(mag)				(erg s ⁻¹)	(M_{\odot})				(cm ⁻²)
(1)	(2)	(3)	(4)	(5)	(6)	(7)	(8)	(9)	(10)	(11)	(12)	(13)	(14)
SWIFT J1416.9–1158		214.2084	-11.9829	0.183	0.0992	1	2018-08-15	45.53	9.05	H β	-1.62	0.79	20.00 ^{+0.00} _{-0.00}
SWIFT J1421.4+4747	SBS 1419+480	215.3742	47.7902	0.048	0.0727	1	2018-08-16	45.27	8.54	H α	-1.37	0.58	20.00 ^{+0.00} _{-0.00}
SWIFT J1424.2+2435	NGC 5610	216.0954	24.6144	0.060	0.0169	2	2018-12-18	43.99	7.81	σ_*	-1.92	0.40	22.56 ^{+0.06} _{-0.10}
SWIFT J1431.2+2816		217.7700	28.2873	0.057	0.0461	1	2019-01-16	44.52	8.93	M_*	-2.51	0.73	20.00 ^{+0.00} _{-0.00}
SWIFT J1457.8–4308	IC 4518A	224.4216	-43.1321	0.429	0.0158	2	2020-06-14	44.18	6.89	M_*	-0.81	0.34	23.36 ^{+0.09} _{-0.08}
SWIFT J1506.7+0353B		226.6840	3.8620	0.132	0.0373	2	2019-01-11	44.62	7.49	σ_*	-0.97	0.88	22.18 ^{+0.07} _{-0.08}
SWIFT J1513.8–8125		228.6751	-81.3939	0.744	0.0687	1	2020-07-02	45.40	8.71	H α	-1.41	0.58	20.00 ^{+0.00} _{-0.00}
SWIFT J1546.3+6928		236.6014	69.4861	0.114	0.0378	2	2021-03-19	44.62	9.18	σ_*	-2.66	0.27	23.49 ^{+0.24} _{-0.18}
SWIFT J1548.5–1344	NGC 5995	237.1040	-13.7578	0.439	0.0244	1	2019-01-18	44.68	7.01	H α	-0.43	0.82	21.97 ^{+0.06} _{-0.07}
SWIFT J1605.9–7250		241.3470	-72.8990	0.257	0.0900	2	2020-07-08	45.66	9.42	M_*	-1.86	0.61	23.18 ^{+0.10} _{-0.10}
SWIFT J1643.2+7036	NGC 6232	250.8343	70.6325	0.121	0.0149	2	2021-05-06	44.15	7.43	σ_*	-1.38	0.85	24.35 ^{+0.43} _{-0.19}
SWIFT J1648.0–3037		252.0635	-30.5845	0.935	0.0310	1	2018-05-27	44.89	7.67	M_*	-0.88	0.58	21.40 ^{+0.29} _{-0.50}
SWIFT J1652.3+5554		253.0780	55.9055	0.053	0.0291	2	2018-08-24	44.37	8.74	M_*	-2.47	0.36	22.70 ^{+0.08} _{-0.07}
SWIFT J1731.3+1442		262.8058	14.7155	0.264	0.0826	1	2021-06-07	45.16	9.00	M_*	-1.94	0.77	20.00 ^{+0.00} _{-0.00}
SWIFT J1737.7–5956A		264.4128	-59.9407	0.205	0.0171	2	2020-09-02	...	8.41	M_*	...	0.81	-9.00 ^{+0.00} _{-0.00}
SWIFT J1741.9–1211	2E 1739.1-1210	265.4802	-12.1991	1.591	0.0369	1	2020-08-01	45.07	8.04	H α	-1.07	0.46	21.40 ^{+0.08} _{-0.08}
SWIFT J1747.7–2253		266.8739	-22.8791	2.794	0.0467	1	2018-08-19	44.93	8.99	H α	-2.16	0.91	22.41 ^{+0.28} _{-0.37}
SWIFT J1747.8+6837A	Mrk 507	267.1599	68.7044	0.106	0.0551	1	2018-11-14	44.35	7.21	H α	-0.96	0.64	20.00 ^{+0.00} _{-0.00}
SWIFT J1747.8+6837B	VII Zw 742	266.7493	68.6102	0.103	0.0630	1	2020-03-15	44.59	7.20	H α	-0.71	0.86	20.00 ^{+0.00} _{-0.00}
SWIFT J1748.8–3257		267.2297	-32.9145	4.482	0.0200	1	2018-07-06	44.43	7.67	H α	-1.34	0.61	21.38 ^{+0.07} _{-0.02}
SWIFT J1800.3+6637		270.0304	66.6151	0.124	0.0265	2	2018-08-19	44.55	8.88	M_*	-2.43	0.62	24.02 ^{+0.23} _{-0.16}
SWIFT J1807.9+1124		271.9580	11.3470	0.365	0.0787	1	2021-06-04	45.45	8.82	H α	-1.47	0.73	21.54 ^{+0.06} _{-0.09}
SWIFT J1824.2+1845		276.0451	18.7691	0.572	0.0661	1	2021-06-13	45.16	7.88	H α	-0.82	0.86	22.43 ^{+0.13} _{-0.12}
SWIFT J1824.3–5624	IC 4709	276.0808	-56.3692	0.242	0.0167	2	2021-05-28	44.36	8.08	M_*	-1.82	0.32	23.15 ^{+0.05} _{-0.07}
SWIFT J1826.8+3254		276.6350	32.8583	0.294	0.0221	2	2018-08-11	44.22	7.72	σ_*	-1.60	0.31	22.98 ^{+0.11} _{-0.10}
SWIFT J1830.8+0928		277.7110	9.4783	0.670	0.0191	2	2020-06-01	43.40	8.39	σ_*	-3.09	0.80	23.18 ^{+0.22} _{-0.28}
SWIFT J1844.5–6221	Fairall 51	281.2249	-62.3648	0.297	0.0139	1	2018-07-25	44.15	7.20	H α	-1.15	0.35	20.00 ^{+0.00} _{-0.00}
SWIFT J1845.4+7211		281.3593	72.1838	0.167	0.0463	2	2018-10-02	44.64	7.86	M_*	-1.32	0.37	22.46 ^{+0.07} _{-0.10}
SWIFT J1848.0–7832		281.7618	-78.5304	0.306	0.0743	1	2019-01-11	45.24	7.73	M_*	-0.59	0.62	20.00 ^{+0.00} _{-0.00}
SWIFT J1856.2–7829		284.2823	-78.4725	0.427	0.0420	1	2020-07-06	44.88	8.76	M_*	-1.98	0.55	22.15 ^{+0.11} _{-0.11}
SWIFT J1903.9+3349	UGC 11397	285.9548	33.8447	0.248	0.0152	2	2019-10-15	43.89	8.24	M_*	-2.45	0.60	22.87 ^{+0.11} _{-0.15}
SWIFT J1905.4+4231		286.3581	42.4610	0.198	0.0279	1	2018-09-24	44.16	8.03	M_*	-1.97	0.55	20.76 ^{+0.42} _{-0.30}

Table 1 continued

Table 1 (*continued*)

Source Name	Alt. Name	R.A.	Dec.	A_V	z	Type	Obs. Date	$\log L_{\text{bol}}$	$\log M_{\text{BH}}$	M	$\log \lambda$	b/a	$\log N_{\text{H}}$
		(deg.)	(deg.)	(mag)				(erg s^{-1})	(M_{\odot})				(cm^{-2})
(1)	(2)	(3)	(4)	(5)	(6)	(7)	(8)	(9)	(10)	(11)	(12)	(13)	(14)
SWIFT J1940.4–3015	IGR J19405-3016	295.0629	-30.2644	0.281	0.0525	1	2020-07-09	45.03	8.37	H α	-1.44	0.76	20.52 $^{+0.08}_{-0.11}$
SWIFT J1947.3+4447		296.8307	44.8284	0.535	0.0528	2	2018-12-05	45.12	9.01	σ_*	-1.99	0.75	22.84 $^{+0.03}_{-0.02}$
SWIFT J1952.4+0237	3C 403	298.0660	2.5070	0.520	0.0584	2	2020-07-19	45.47	9.15	σ_*	-1.78	0.87	23.69 $^{+0.13}_{-0.04}$
SWIFT J2006.5+5619		301.6389	56.3435	1.013	0.0423	2	2019-01-11	44.66	7.82	M_*	-1.26	0.22	23.48 $^{+0.09}_{-0.10}$
SWIFT J2010.7+4801		302.5725	48.0059	1.106	0.0254	2	2018-12-05	44.18	9.48	σ_*	-3.40	0.59	23.00 $^{+0.17}_{-0.43}$
SWIFT J2018.4–5539	PKS 2014-55	304.5050	-55.6590	0.184	0.0607	2	2020-07-10	45.39	8.50	M_*	-1.21	0.63	23.45 $^{+0.10}_{-0.08}$
SWIFT J2018.8+4041		304.6613	40.6834	9.336	0.0144	2	2019-01-17	44.01	7.85	M_*	-1.94	0.87	22.78 $^{+0.04}_{-0.06}$
SWIFT J2021.9+4400		305.4544	44.0110	3.620	0.0175	2	2018-12-05	43.85	7.52	M_*	-1.77	0.52	23.02 $^{+0.34}_{-0.24}$
SWIFT J2027.1–0220		306.7328	-2.2775	0.254	0.0291	2	2018-07-26	44.53	7.83	M_*	-1.40	0.94	23.82 $^{+0.15}_{-0.11}$
SWIFT J2035.2+2604		308.7735	26.0583	0.746	0.0478	1	2018-09-30	44.67	7.53	H α	-0.96	0.26	21.30 $^{+0.34}_{-0.29}$
SWIFT J2040.2–5126	ESO 234-IG 063	310.0656	-51.4297	0.077	0.0541	2	2021-05-22	44.91	8.11	σ_*	-1.30	0.73	23.41 $^{+0.20}_{-0.18}$
SWIFT J2044.0+2832	RX J2044.0+2833	311.0188	28.5534	0.941	0.0489	1	2018-10-04	44.93	8.23	H α	-1.40	0.64	21.15 $^{+0.12}_{-0.09}$
SWIFT J2052.0–5704	IC 5063	313.0098	-57.0688	0.169	0.0115	2	2019-11-25	44.31	8.17	M_*	-1.96	0.83	23.56 $^{+0.07}_{-0.01}$
SWIFT J2109.1–0942		317.2915	-9.6707	0.584	0.0268	1	2018-09-18	44.40	7.52	H α	-1.22	0.87	21.20 $^{+0.32}_{-0.50}$
SWIFT J2114.4+8206		318.5049	82.0801	0.419	0.0833	1	2018-04-02	45.68	9.02	H α	-1.44	0.82	20.00 $^{+0.00}_{-0.00}$
SWIFT J2118.9+3336		319.8714	33.5491	0.589	0.0509	1	2019-01-03	44.77	8.11	H α	-1.44	0.74	21.57 $^{+0.17}_{-0.17}$
SWIFT J2124.6+5057	4C 50.55	321.1643	50.9735	6.665	0.0151	1	2018-12-13	44.95	6.69	H α	0.16	0.70	23.02 $^{+0.08}_{-0.14}$
SWIFT J2127.4+5654		321.9391	56.9430	3.523	0.0147	1	2018-08-19	44.15	6.60	M_*	-0.55	0.83	20.00 $^{+0.00}_{-0.00}$
SWIFT J2156.1+4728		323.9750	47.4727	1.741	0.0253	1	2018-12-06	44.39	7.47	H α	-1.18	0.34	21.28 $^{+0.24}_{-0.10}$
SWIFT J2201.9–3152	NGC 7172	330.5080	-31.8698	0.073	0.0083	2	2020-09-15	44.22	8.45	σ_*	-2.33	0.70	22.91 $^{+0.01}_{-0.01}$
SWIFT J2204.7+0337		331.0799	3.5639	0.126	0.0611	2	2020-07-19	45.10	8.25	M_*	-1.25	0.96	22.83 $^{+0.15}_{-0.14}$
SWIFT J2214.2–2557		333.5382	-25.9636	0.065	0.0519	2	2020-09-16	44.89	8.17	σ_*	-1.38	0.83	23.48 $^{+0.23}_{-0.12}$
SWIFT J2219.7+2614		334.9573	26.2244	0.297	0.0877	1	2019-01-20	45.41	9.01	H α	-1.70	0.67	21.52 $^{+0.06}_{-0.04}$
SWIFT J2237.0+2543		339.1370	25.7632	0.143	0.0246	2	2018-04-27	44.07	8.43	M_*	-2.46	0.91	23.02 $^{+0.18}_{-0.09}$
SWIFT J2246.0+3941	3C 452	341.4532	39.6877	0.381	0.0811	1	2018-12-08	45.66	6.58	H α	0.98	0.70	23.76 $^{+0.07}_{-0.08}$
SWIFT J2320.8+6434		350.1526	64.5125	4.592	0.0717	2	2019-10-23	45.03	7.65	M_*	-0.72	0.57	22.04 $^{+0.41}_{-0.19}$
SWIFT J2330.5+7124	IGR J23308+7120	352.6571	71.3796	1.791	0.0369	2	2018-12-15	44.40	8.55	M_*	-2.25	0.95	22.95 $^{+0.06}_{-0.06}$
SWIFT J2359.3–6058		359.7682	-60.9165	0.037	0.0963	2	2020-01-14	45.40	8.92	M_*	-1.62	0.57	23.16 $^{+0.02}_{-0.02}$

Table 1 *continued*

Table 1 (*continued*)

Source Name	Alt. Name	R.A.	Dec.	A_V	z	Type	Obs. Date	$\log L_{\text{bol}}$	$\log M_{\text{BH}}$	M	$\log \lambda$	b/a	$\log N_{\text{H}}$
		(deg.)	(deg.)	(mag)				(erg s^{-1})	(M_{\odot})				(cm^{-2})
(1)	(2)	(3)	(4)	(5)	(6)	(7)	(8)	(9)	(10)	(11)	(12)	(13)	(14)

NOTE— Col. (1): Object name. Col. (2): Alternative name. Col. (3): Right Ascension in J2000 coordinates. Col. (4): Declination in J2000 coordinates. Col. (5): Galactic extinction in the V band. Col. (6): Redshift. Col. (7): AGN type determined based on the optical spectrum. Col. (8): Observation date. Col. (9): Bolometric luminosity inferred from the intrinsic X-ray luminosity, assuming a bolometric correction of 8 (Ricci et al. 2017). Col. (10): Black hole mass. Col. (11): Method to estimate the black hole mass: $\text{H}\alpha$: virial method with the broad $\text{H}\alpha$; $\text{H}\beta$: virial method with the broad $\text{H}\beta$; σ_* : $M_{\text{BH}} - \sigma_*$ relation; M_* : $M_{\text{BH}} - M_*$ relation. Col. (12): Eddington ratio ($\lambda = L_{\text{bol}}/L_{\text{Edd}}$). Col. (13): Axis ratio. Col. (14): Column density of neutral hydrogen derived from the hard X-ray spectrum (Ricci et al. 2017).

Table 2. Morphology of Host Galaxies

Source Name	Morp.(1)	Morp.(2)	T/S	Major/Minor	Merging Stage	Nucleus
(1)	(2)	(3)	(4)	(5)	(6)	(7)
SWIFT J0001.0–0708	S0	Sb	m1	s
SWIFT J0001.6–7701	SB	Sc	T	Minor	m2	s
SWIFT J0003.3+2737	SA	Sa	T	Minor	m2	s
SWIFT J0005.0+7021	E/S0	...	S	s
SWIFT J0006.2+2012	E	Minor	m1	s
SWIFT J0036.3+4540	SA	Sc	m1	s
SWIFT J0100.9–4750	SA	Sa	T	Major	m3	s
SWIFT J0123.9–5846	SB	Sb	S	Minor	m2	s
SWIFT J0128.4+1631	SB	Sc	s
SWIFT J0134.1–3625	E	s
SWIFT J0157.2+4715	SB	Sc	T	Minor	m2	s
SWIFT J0202.4+6824A	SB	Sb	s
SWIFT J0202.4+6824B	SB	Sb	s
SWIFT J0206.2–0019	pec.	...	T	Major	m4	s
SWIFT J0234.6–0848	pec.	...	T	Major	m4	d
SWIFT J0243.9+5324	SB	Sb	s
SWIFT J0333.3+3720	S0	Sa	S	Minor	m1	s
SWIFT J0347.0–3027	S0	Sa	s
SWIFT J0356.9–4041	E/S0	Sa	s
SWIFT J0405.3–3707	E/S0	Sa	s
SWIFT J0429.6–2114	pec.	...	T	Major	m4	s
SWIFT J0443.9+2856	SB	Sb	s
SWIFT J0446.4+1828	SB	Sb	s
SWIFT J0456.3–7532	SB0	Sa	s
SWIFT J0504.6–7345	SA	Sb	s
SWIFT J0510.7+1629	E/S0	s
SWIFT J0516.2–0009	SA	Sa	s
SWIFT J0526.2–2118	SB0	Sa	S	Minor	...	s
SWIFT J0528.1–3933	SB	Sa	T	Major	m2	dd
SWIFT J0533.9–1318	S0	Sa	s
SWIFT J0544.4–4328	E	...	T	Minor	m2	s
SWIFT J0552.5+5929	pec.	...	T	Major	m4	s
SWIFT J0623.9–6058	SB	Sa	T	Minor	m1	s
SWIFT J0641.3+3257	S0	Sa	T	Major	m1	s
SWIFT J0645.9+5303	SA	Sa	s
SWIFT J0707.1+6433	E/S0	Sa	S	Minor	m1	s
SWIFT J0709.0–4642	E	...	S	Minor	m1	s
SWIFT J0736.9+5846	SB	Sc	s
SWIFT J0743.0+6513	E/S0	Sa	s
SWIFT J0743.3–2546	SB	Sc	s
SWIFT J0747.5+6057	SB	Sb	s
SWIFT J0747.6–7326	S0	Sa	s
SWIFT J0753.1+4559	E	s

Table 2 *continued*

Table 2 (*continued*)

Source Name	Morp.(1)	Morp.(2)	T/S	Major/Minor	Merging Stage	Nucleus
(1)	(2)	(3)	(4)	(5)	(6)	(7)
SWIFT J0756.3–4137	E	s
SWIFT J0759.8–3844	E	s
SWIFT J0800.1+2638	SB	Sb	m1	s
SWIFT J0801.9–4946	SA	Sc	s
SWIFT J0804.6+1045	pec.	...	T	Major	m4	s
SWIFT J0805.1–0110	SA	Sa	s
SWIFT J0807.9+3859	SB	Sa	s
SWIFT J0819.2–2259	SB	Sa	s
SWIFT J0823.4–0457	SA	Sa	m1	s
SWIFT J0840.2+2947	E/S0	Sa	S	Minor	m2	s
SWIFT J0855.6+6425	SA	Sa	s
SWIFT J0902.7–4814	E	s
SWIFT J0923.7+2255	SB	Sb	s
SWIFT J0924.2–3141	E	s
SWIFT J0925.2–8423	E	...	T	Minor	m2	s
SWIFT J0936.2–6553	SB0	Sa	s
SWIFT J0942.2+2344	SB0	Sa	s
SWIFT J0947.6–3057	SB0	Sa	s
SWIFT J1020.5–0237B	SB	Sb	m1	s
SWIFT J1021.7–0327	E	s
SWIFT J1029.8–3821	SA	Sa	m1	s
SWIFT J1031.9–1418	E	m1	s
SWIFT J1032.7–2835	S0	Sb	s
SWIFT J1033.6+7303	E/S0	Sa	s
SWIFT J1038.8–4942	E	s
SWIFT J1040.7–4619	S0	Sa	s
SWIFT J1042.4+0046	SA	Sb	m1	s
SWIFT J1043.4+1105	E	s
SWIFT J1059.8+6507	pec.	...	T	Minor	m3	s
SWIFT J1132.9+1019A	SB	Sc	s
SWIFT J1136.7–6007	S0	Sb	s
SWIFT J1139.1+5913	E/S0	...	S	Minor	m2	s
SWIFT J1143.7+7942	SB0	Sa	s
SWIFT J1148.3+0901	SB0	Sa	m1	s
SWIFT J1200.2–5350	pec.	...	S	...	m4	s
SWIFT J1211.3–3935	SB	Sb	s
SWIFT J1213.1+3239A	S0	Sb	s
SWIFT J1217.2–2611	SB	Sb	T	Major	m2	s
SWIFT J1248.2–5828	S0	Sb	T	Major	m2	s
SWIFT J1306.4–4025B	SB0	Sa	s
SWIFT J1315.8+4420	pec.	...	T	Major	m3	s
SWIFT J1316.9–7155	E	s
SWIFT J1322.2–1641	SB	Sb	s
SWIFT J1332.0–7754	SA	Sa	s
SWIFT J1333.5–3401	SA	Sc	s
SWIFT J1336.0+0304	SA	Sb	s

Table 2 *continued*

Table 2 (*continued*)

Source Name	Morp.(1)	Morp.(2)	T/S	Major/Minor	Merging Stage	Nucleus
(1)	(2)	(3)	(4)	(5)	(6)	(7)
SWIFT J1338.2+0433	S0	Sa	s
SWIFT J1341.5+6742	SB0	Sa	m1	s
SWIFT J1345.5+4139	SA	Sc	s
SWIFT J1349.7+0209	S0	Sa	m1	s
SWIFT J1354.5+1326	SA	Sb	T	Major	m3	s
SWIFT J1416.9-1158	E	s
SWIFT J1421.4+4747	E/S0	Sa	...	Minor	m1	s
SWIFT J1424.2+2435	SB	Sb	...	Minor	...	s
SWIFT J1431.2+2816	SB	Sc	m1	s
SWIFT J1457.8-4308	pec.	...	T	Major	m3	dd
SWIFT J1506.7+0353B	SB0	Sa	s
SWIFT J1513.8-8125	S0	Sa	T	Major	m3	dd
SWIFT J1546.3+6928	SB0	Sb	m1	s
SWIFT J1548.5-1344	SB	Sc	s
SWIFT J1605.9-7250	SA	Sb	s
SWIFT J1643.2+7036	SB	Sa	s
SWIFT J1648.0-3037	E	s
SWIFT J1652.3+5554	SB	Sc	s
SWIFT J1731.3+1442	SA	Sa	T	s
SWIFT J1737.7-5956A	SA	Sb	s
SWIFT J1741.9-1211	SB	Sa	s
SWIFT J1747.7-2253	E	s
SWIFT J1747.8+6837A	SB	Sb	m1	s
SWIFT J1747.8+6837B	E	...	T	Major	m3	dd
SWIFT J1748.8-3257	E/S0	s
SWIFT J1800.3+6637	SB	Sb	s
SWIFT J1807.9+1124	E	s
SWIFT J1824.2+1845	SA	Sa	s
SWIFT J1824.3-5624	SA	Sa	s
SWIFT J1826.8+3254	S0	Sa	s
SWIFT J1830.8+0928	SB0	Sa	s
SWIFT J1844.5-6221	SB	Sb	s
SWIFT J1845.4+7211	pec.	...	T	Major	m4	d
SWIFT J1848.0-7832	pec.	...	T	Major	m4	d
SWIFT J1856.2-7829	S0	Sb	s
SWIFT J1903.9+3349	SB	Sa	s
SWIFT J1905.4+4231	SB	Sa	s
SWIFT J1940.4-3015	SB	Sc	s
SWIFT J1947.3+4447	SA	Sa	s
SWIFT J1952.4+0237	E	s
SWIFT J2006.5+5619	SA	Sa	s
SWIFT J2010.7+4801	SB0	Sa	s
SWIFT J2018.4-5539	E/S0	s
SWIFT J2018.8+4041	SA	Sc	s
SWIFT J2021.9+4400	SB0	Sa	s
SWIFT J2027.1-0220	S0	Sa	s

Table 2 *continued*

Table 2 (*continued*)

Source Name	Morp.(1)	Morp.(2)	T/S	Major/Minor	Merging Stage	Nucleus
(1)	(2)	(3)	(4)	(5)	(6)	(7)
SWIFT J2035.2+2604	SA	Sa	s
SWIFT J2040.2–5126	pec.	...	T	Major	m4	s
SWIFT J2044.0+2832	SB	Sa	s
SWIFT J2052.0–5704	E	s
SWIFT J2109.1–0942	SB	Sa	s
SWIFT J2114.4+8206	E	s
SWIFT J2118.9+3336	E	...	S	Minor	m1	s
SWIFT J2124.6+5057	E	s
SWIFT J2127.4+5654	E	s
SWIFT J2156.1+4728	SA	Sc	s
SWIFT J2201.9–3152	E/S0	s
SWIFT J2204.7+0337	pec.	...	T	Minor	m4	s
SWIFT J2214.2–2557	SB	Sb	s
SWIFT J2219.7+2614	E	...	S	Minor	m1	s
SWIFT J2237.0+2543	SB	Sb	s
SWIFT J2246.0+3941	E	s
SWIFT J2320.8+6434	E	s
SWIFT J2330.5+7124	SB	Sa	s
SWIFT J2359.3–6058	E	s

NOTE— Col. (1): Object name. Col. (2): Morphological classification: E;E/S0;S0;SB0;SA;SB;peculiar. Col. (3): Morphological classification based on the bulge dominance: Sa/Sb/Sc. Col. (4): Presence of perturbed structure: “T” = tidal tail; “S” = shell structure. Col. (5): Merging feature: “Major” = major merger; “Minor” = minor merger. Col. (6): Merging stage: “m1” = a companion galaxy with very faint (or no) sign of interaction; “m2” = a sign of interaction (tail and shell) but no major disturbance in the host galaxy; “m3” = major disturbance in the host galaxy but the companion galaxy is not yet merged. “m4” = two galaxies share the common envelope (latest stage of the merger). Col. (7): Number of nuclei: “s” = single nucleus; “d” = double nuclei in a single host; “dd” = double nuclei in separate hosts.

Table 3. Merging Fraction

Parameter	Bin	Tidal/shell			Major/minor			m2+m3+m4			Double nuclei		
		All	Type 1	Type 2	All	Type 1	Type 2	All	Type 1	Type 2	All	Type 1	Type 2
(1)	(2)	(3)	(4)	(5)	(6)	(7)	(8)	(9)	(10)	(11)	(12)	(13)	(14)
$\log L_{\text{bol}}$	43.25	$0.00^{+0.17}_{-0.00}$	$0.00^{+0.54}_{-0.00}$	$0.00^{+0.21}_{-0.00}$	$0.00^{+0.17}_{-0.00}$	$0.00^{+0.54}_{-0.00}$	$0.00^{+0.21}_{-0.00}$	$0.00^{+0.17}_{-0.00}$	$0.00^{+0.54}_{-0.00}$	$0.00^{+0.21}_{-0.00}$	$0.00^{+0.17}_{-0.00}$	$0.00^{+0.54}_{-0.00}$	$0.00^{+0.21}_{-0.00}$
	43.75	$0.00^{+0.07}_{-0.00}$	$0.00^{+0.35}_{-0.00}$	$0.00^{+0.08}_{-0.00}$	$0.08^{+0.11}_{-0.04}$	$0.00^{+0.35}_{-0.00}$	$0.09^{+0.12}_{-0.05}$	$0.00^{+0.07}_{-0.00}$	$0.00^{+0.35}_{-0.00}$	$0.00^{+0.08}_{-0.00}$	$0.00^{+0.07}_{-0.00}$	$0.00^{+0.35}_{-0.00}$	$0.00^{+0.08}_{-0.00}$
	44.25	$0.13^{+0.06}_{-0.04}$	$0.00^{+0.06}_{-0.00}$	$0.22^{+0.10}_{-0.07}$	$0.15^{+0.07}_{-0.05}$	$0.06^{+0.09}_{-0.04}$	$0.22^{+0.10}_{-0.07}$	$0.10^{+0.06}_{-0.04}$	$0.00^{+0.06}_{-0.00}$	$0.17^{+0.09}_{-0.06}$	$0.05^{+0.05}_{-0.02}$	$0.00^{+0.06}_{-0.00}$	$0.09^{+0.08}_{-0.04}$
	44.75	$0.33^{+0.07}_{-0.06}$	$0.21^{+0.08}_{-0.06}$	$0.48^{+0.10}_{-0.10}$	$0.31^{+0.07}_{-0.06}$	$0.21^{+0.08}_{-0.06}$	$0.43^{+0.10}_{-0.10}$	$0.27^{+0.07}_{-0.06}$	$0.17^{+0.08}_{-0.06}$	$0.39^{+0.10}_{-0.09}$	$0.04^{+0.04}_{-0.02}$	$0.03^{+0.05}_{-0.02}$	$0.04^{+0.06}_{-0.03}$
	45.25	$0.41^{+0.08}_{-0.08}$	$0.52^{+0.10}_{-0.10}$	$0.25^{+0.12}_{-0.09}$	$0.38^{+0.08}_{-0.07}$	$0.48^{+0.10}_{-0.10}$	$0.25^{+0.12}_{-0.09}$	$0.26^{+0.07}_{-0.06}$	$0.30^{+0.10}_{-0.09}$	$0.19^{+0.11}_{-0.08}$	$0.08^{+0.05}_{-0.03}$	$0.13^{+0.09}_{-0.05}$	$0.00^{+0.06}_{-0.00}$
	45.75	$0.00^{+0.17}_{-0.00}$	$0.00^{+0.21}_{-0.00}$	$0.00^{+0.54}_{-0.00}$	$0.00^{+0.17}_{-0.00}$	$0.00^{+0.21}_{-0.00}$	$0.00^{+0.54}_{-0.00}$	$0.00^{+0.17}_{-0.00}$	$0.00^{+0.21}_{-0.00}$	$0.00^{+0.54}_{-0.00}$	$0.00^{+0.17}_{-0.00}$	$0.00^{+0.21}_{-0.00}$	$0.00^{+0.54}_{-0.00}$
$\log \lambda$	-3.50	$0.00^{+0.15}_{-0.00}$	$0.00^{+0.00}_{-0.00}$	$0.00^{+0.15}_{-0.00}$	$0.00^{+0.15}_{-0.00}$	$0.00^{+0.00}_{-0.00}$	$0.00^{+0.15}_{-0.00}$	$0.00^{+0.15}_{-0.00}$	$0.00^{+0.00}_{-0.00}$	$0.00^{+0.15}_{-0.00}$	$0.00^{+0.15}_{-0.00}$	$0.00^{+0.00}_{-0.00}$	$0.00^{+0.15}_{-0.00}$
	-2.50	$0.16^{+0.09}_{-0.06}$	$0.14^{+0.18}_{-0.08}$	$0.17^{+0.10}_{-0.07}$	$0.16^{+0.09}_{-0.06}$	$0.14^{+0.18}_{-0.08}$	$0.17^{+0.10}_{-0.07}$	$0.12^{+0.08}_{-0.05}$	$0.14^{+0.18}_{-0.08}$	$0.11^{+0.09}_{-0.05}$	$0.00^{+0.04}_{-0.00}$	$0.00^{+0.13}_{-0.00}$	$0.00^{+0.05}_{-0.00}$
	-1.50	$0.31^{+0.69}_{-0.06}$	$0.30^{+0.07}_{-0.06}$	$0.31^{+0.07}_{-0.06}$	$0.32^{+0.68}_{-0.06}$	$0.32^{+0.07}_{-0.06}$	$0.31^{+0.07}_{-0.06}$	$0.22^{+0.78}_{-0.06}$	$0.19^{+0.06}_{-0.05}$	$0.25^{+0.07}_{-0.06}$	$0.04^{+0.96}_{-0.02}$	$0.04^{+0.04}_{-0.00}$	$0.04^{+0.04}_{-0.02}$
	-0.50	$0.21^{+0.09}_{-0.07}$	$0.17^{+0.10}_{-0.07}$	$0.33^{+0.20}_{-0.15}$	$0.17^{+0.09}_{-0.06}$	$0.11^{+0.09}_{-0.05}$	$0.33^{+0.20}_{-0.15}$	$0.17^{+0.09}_{-0.06}$	$0.11^{+0.09}_{-0.05}$	$0.33^{+0.20}_{-0.15}$	$0.12^{+0.08}_{-0.05}$	$0.11^{+0.09}_{-0.05}$	$0.17^{+0.20}_{-0.10}$
	0.50	$0.00^{+0.35}_{-0.00}$	$0.00^{+0.35}_{-0.00}$	$0.00^{+0.00}_{-0.00}$	$0.00^{+0.35}_{-0.00}$	$0.00^{+0.35}_{-0.00}$	$0.00^{+0.00}_{-0.00}$	$0.00^{+0.35}_{-0.00}$	$0.00^{+0.35}_{-0.00}$	$0.00^{+0.00}_{-0.00}$	$0.00^{+0.35}_{-0.00}$	$0.00^{+0.35}_{-0.00}$	$0.00^{+0.00}_{-0.00}$
	1.50	$0.00^{+0.54}_{-0.00}$	$0.00^{+0.54}_{-0.00}$	$0.00^{+0.00}_{-0.00}$	$0.00^{+0.54}_{-0.00}$	$0.00^{+0.54}_{-0.00}$	$0.00^{+0.00}_{-0.00}$	$0.00^{+0.54}_{-0.00}$	$0.00^{+0.54}_{-0.00}$	$0.00^{+0.00}_{-0.00}$	$0.00^{+0.54}_{-0.00}$	$0.00^{+0.54}_{-0.00}$	$0.00^{+0.00}_{-0.00}$
$\log N_{\text{H}}$	20.00	$0.32^{+0.08}_{-0.07}$	$0.33^{+0.08}_{-0.07}$	$0.00^{+0.54}_{-0.00}$	$0.35^{+0.08}_{-0.07}$	$0.36^{+0.08}_{-0.07}$	$0.00^{+0.54}_{-0.00}$	$0.27^{+0.08}_{-0.07}$	$0.28^{+0.08}_{-0.07}$	$0.00^{+0.54}_{-0.00}$	$0.08^{+0.06}_{-0.03}$	$0.08^{+0.06}_{-0.03}$	$0.00^{+0.54}_{-0.00}$
	20.50	$0.30^{+0.07}_{-0.06}$	$0.31^{+0.07}_{-0.07}$	$0.00^{+0.54}_{-0.00}$	$0.33^{+0.07}_{-0.07}$	$0.33^{+0.08}_{-0.07}$	$0.00^{+0.54}_{-0.00}$	$0.26^{+0.07}_{-0.06}$	$0.26^{+0.07}_{-0.06}$	$0.00^{+0.54}_{-0.00}$	$0.09^{+0.05}_{-0.03}$	$0.10^{+0.05}_{-0.04}$	$0.00^{+0.54}_{-0.00}$
	21.00	$0.12^{+0.10}_{-0.06}$	$0.12^{+0.10}_{-0.06}$	$0.00^{+0.00}_{-0.00}$	$0.12^{+0.10}_{-0.06}$	$0.12^{+0.10}_{-0.06}$	$0.00^{+0.00}_{-0.00}$	$0.06^{+0.08}_{-0.03}$	$0.06^{+0.08}_{-0.03}$	$0.00^{+0.00}_{-0.00}$	$0.06^{+0.08}_{-0.03}$	$0.06^{+0.08}_{-0.03}$	$0.00^{+0.00}_{-0.00}$
	21.50	$0.20^{+0.10}_{-0.07}$	$0.19^{+0.11}_{-0.08}$	$0.25^{+0.25}_{-0.14}$	$0.20^{+0.10}_{-0.07}$	$0.19^{+0.11}_{-0.08}$	$0.25^{+0.25}_{-0.14}$	$0.05^{+0.07}_{-0.03}$	$0.00^{+0.06}_{-0.00}$	$0.25^{+0.25}_{-0.14}$	$0.05^{+0.07}_{-0.03}$	$0.00^{+0.06}_{-0.00}$	$0.25^{+0.25}_{-0.14}$
	22.00	$0.25^{+0.08}_{-0.07}$	$0.21^{+0.13}_{-0.09}$	$0.28^{+0.11}_{-0.09}$	$0.22^{+0.08}_{-0.06}$	$0.21^{+0.13}_{-0.09}$	$0.22^{+0.11}_{-0.08}$	$0.16^{+0.07}_{-0.05}$	$0.07^{+0.10}_{-0.04}$	$0.22^{+0.11}_{-0.08}$	$0.06^{+0.06}_{-0.03}$	$0.00^{+0.07}_{-0.00}$	$0.11^{+0.09}_{-0.05}$
	22.50	$0.26^{+0.07}_{-0.06}$	$0.17^{+0.13}_{-0.08}$	$0.29^{+0.08}_{-0.07}$	$0.24^{+0.07}_{-0.06}$	$0.08^{+0.11}_{-0.05}$	$0.29^{+0.08}_{-0.07}$	$0.22^{+0.07}_{-0.05}$	$0.08^{+0.11}_{-0.05}$	$0.26^{+0.08}_{-0.07}$	$0.02^{+0.03}_{-0.01}$	$0.00^{+0.08}_{-0.00}$	$0.03^{+0.04}_{-0.02}$
	23.00	$0.31^{+0.07}_{-0.06}$	$0.20^{+0.22}_{-0.12}$	$0.32^{+0.07}_{-0.07}$	$0.31^{+0.07}_{-0.06}$	$0.00^{+0.17}_{-0.00}$	$0.34^{+0.07}_{-0.07}$	$0.22^{+0.06}_{-0.05}$	$0.00^{+0.17}_{-0.00}$	$0.25^{+0.07}_{-0.06}$	$0.02^{+0.03}_{-0.01}$	$0.00^{+0.17}_{-0.00}$	$0.02^{+0.03}_{-0.01}$
	23.50	$0.23^{+0.07}_{-0.06}$	$0.00^{+0.17}_{-0.00}$	$0.26^{+0.08}_{-0.07}$	$0.23^{+0.07}_{-0.06}$	$0.00^{+0.17}_{-0.00}$	$0.26^{+0.08}_{-0.07}$	$0.15^{+0.07}_{-0.05}$	$0.00^{+0.17}_{-0.00}$	$0.18^{+0.07}_{-0.06}$	$0.03^{+0.04}_{-0.01}$	$0.00^{+0.17}_{-0.00}$	$0.03^{+0.04}_{-0.02}$
	24.00	$0.06^{+0.08}_{-0.03}$	$0.00^{+0.26}_{-0.04}$	$0.07^{+0.09}_{-0.04}$	$0.06^{+0.08}_{-0.03}$	$0.00^{+0.26}_{-0.00}$	$0.07^{+0.09}_{-0.04}$	$0.06^{+0.08}_{-0.03}$	$0.00^{+0.26}_{-0.00}$	$0.07^{+0.09}_{-0.04}$	$0.00^{+0.05}_{-0.00}$	$0.00^{+0.26}_{-0.00}$	$0.00^{+0.06}_{-0.00}$
	24.50	$0.00^{+0.17}_{-0.00}$	$0.00^{+0.17}_{-0.00}$	$0.00^{+0.17}_{-0.00}$	$0.00^{+0.17}_{-0.00}$	$0.00^{+0.17}_{-0.00}$	$0.00^{+0.17}_{-0.00}$	$0.00^{+0.17}_{-0.00}$	$0.00^{+0.17}_{-0.00}$	$0.00^{+0.17}_{-0.00}$	$0.00^{+0.17}_{-0.00}$	$0.00^{+0.17}_{-0.00}$	$0.00^{+0.17}_{-0.00}$

NOTE— Col. (1): Parameter. Col. (2): Bin. The units for L_{bol} and N_{H} are erg s^{-1} and cm^{-2} , respectively. Col. (3): Merging fraction of the entire sample, based on the presence of tidal tail or shell. Col. (4): Merging fraction of type 1 AGN, based on the presence of tidal tail or shell. Col. (5): Merging fraction of type 2 AGN, based on the presence of tidal tail or shell. Col. (6): Merging fraction of the entire sample, based on the presence of major/minor merging features. Col. (7): Merging fraction of type 1 AGN, based on the presence of major/minor merging features. Col. (8): Merging fraction of type 2 AGN, based on the presence of major/minor merging features. Col. (9): Merging fraction of the entire sample, based on the merging stage (m2+m3+m4). Col. (10): Merging fraction of type 1 AGN, based on the merging stage (m2+m3+m4). Col. (11): Merging fraction of type 2 AGN, based on the merging stage (m2+m3+m4). Col. (12): Fraction of the entire sample, based on the presence of double nuclei. Col. (13): Fraction of type 1 AGN, based on the presence of double nuclei. Col. (14): Fraction of type 2 AGN, based on the presence of double nuclei.